

Level 2 Photometric Calibration for the LSST Survey

R. Lynne Jones¹, Željko Ivezić¹, Tim Axelrod², David Burke³,
James G. Bartlett⁴, Gurvan Bazin⁴, Guillaume Blanc⁴, Alexandre Boucaud⁴, Michel Crézé⁴,
Cécile Roucelle⁴, Abhijit Saha⁵, J. Allyn Smith⁷ Michael A. Strauss⁶
on behalf of The Photometric Calibration Team

Docushare-8123, –/–/–

ABSTRACT

This document describes the photometric calibration procedure for LSST Data Release catalogs. This procedure will use specialized hardware, an auxiliary telescope, an atmospheric water vapor measurement system, and narrow-band dome screen illuminator, to measure the wavelength dependence of the atmospheric and hardware response functions, together with a self-calibration procedure that leverages multiple observations of the same sources over many epochs, to deliver 1%-level photometry across the observed sky.

Contents

1	Introduction	4
2	Photometric Requirements	5
3	The Photometric Calibration Process	7

¹University of Washington

²University of Arizona

³SLAC National Accelerator Laboratory

⁴APC, Université Paris Diderot

⁵NOAO

⁶Princeton University

⁷Austin Peay State University

4 From Flux to Counts	9
4.1 Normalized bandpass response, $\phi_b(\lambda)$	15
4.2 Perturbations to the System Bandpass	17
4.3 Effects of Atmospheric Variations	18
4.4 Throughput Variations Due to Contamination	24
4.5 Variations in Detector Quantum Efficiency	24
4.6 Throughput Variations Due to Filter Position Shifts	24
4.7 Putting it All Together	24
5 From Counts to Flux	28
5.1 Measuring the Hardware Response	31
5.1.1 Determining the Illumination Correction	31
5.2 Measuring the Atmospheric Transmission	36
5.3 Self Calibration	36
5.3.1 Photometric vs. Non-photometric data	43
5.4 Calibration Operations	43
6 Fixing LSST to an external scale	44
6.1 Band to band (color)	45
6.2 Single bandpass to external flux system (absolute scale)	46
7 Calibration Hardware	46
7.1 Flat Field Illumination System	46
7.2 Auxiliary Telescope	47
The expected effect of $\phi_b^{atm}(\lambda)$ variations	48
7.3 Water Vapor Monitoring System	49
7.4 Camera System Telemetry	49

8 Calibration Error Budget	49
8.1 Repeatability Errors	49
8.1.1 Errors in m_b^{inst}	55
8.1.2 Errors in Δm_b^{obs}	55
8.1.3 Errors in Z_b^{obs}	57
8.2 Uniformity Errors	58
9 Testing and Verification	58
9.1 Self Calibration Simulation	60
9.2 Auxiliary Telescope Simulation	60
9.3 Calibration Performance Metrics	60
9.3.1 Repeatability	60
9.3.2 Spatial Uniformity	60
9.3.3 Flux Calibration	60
9.3.4 Color Calibration	60
10 Software Implementation	61
10.1 Level 2 Data Products	61
11 Risks and Mitigations	61
A Filter Set	64
B Photometric measurements for non-main sequence stars	64
C Glossary	65

1. Introduction

LSST is required to deliver 1%-level photometry across the observed sky and under a wide range of observing conditions (0.5%-level for repeat observations of the same source). This represents about a factor of two improvement over the current state-of-the-art wide-field optical photometry delivered by SDSS under photometric conditions. This factor of two improvement will have a major impact on science deliverables because it implies that the error volume in the five-dimensional LSST color space will be over thirty times smaller than for SDSS-like photometry. This smaller error volume will improve source classification and the precision of quantities such as photometric redshifts for galaxies and photometric metallicity for stars. For example, a given spectral energy distribution (SED) corresponding to some galaxy type produces a line in the *ugrizy* multi-dimensional color space when redshifted, where the position of the galaxy along that line in *ugrizy* space is a function of redshift. Different galaxy SEDs produce lines that are often close to each other in *ugrizy* space and sometimes even cross. The smaller the error volume around an observed galaxy’s measured *ugrizy* colors, the smaller the number of different lines (thus, different SEDs) and different positions along the line (thus, different redshifts) which will be consistent with the measurement. The same conclusion is valid in the case of algorithms that estimate stellar effective temperature and metallicity, as well as any other model-based interpretation of measurements. Furthermore, the smaller error volume per source is advantageous even in the absence of any models. Two sources whose color differences produce a value of χ^2 per degree of freedom of 1, will have a χ^2 per degree of freedom of 4 when the errors are halved. In case of five degrees of freedom, $\chi^2 \text{ pdf} > 4$ will happen by chance in only 0.1% of all cases. Therefore, the ability to reliably detect color differences between sources is a strong function of photometric errors.

The factor of two reduction in photometric error results from two major differences between LSST and SDSS. First, each source will receive hundreds of observations over the ten years of the LSST survey. These series of repeat observations will be used to self-calibrate the photometric system across the sky and for each observation (akin, but not identical to, the uber-calibration procedure used by SDSS (Padmanabhan et al. 2008)), allowing LSST to operate in a wide variety of conditions. Secondly, the wavelength dependence of the hardware and atmospheric transmission response functions will be measured with auxiliary instrumentation on sufficiently fine angular and temporal scales to enable their explicit inclusion in the calibration procedure, rather than resorting to traditional approximations such as linear color terms. SNLS re-processing of CFHT Legacy Survey data found these color-dependent terms to be a significant contributor to the photometric calibration process (Regnault et al. 2009), on the level of a few to several percent. **TODO here on why it’s hard - drift scan and all weather**

This document describes the calibration requirements and processes for LSST Data Release photometry. At each Data Release, there will be a complete recalibration of all data acquired to that point, on approximately an annual schedule. These data products are referred to as Level 2 Data Products. There will also be a real-time data calibration process, based on the best available set of prior calibrated observations, to provide real-time, but lower quality, photometry for quality assurance, generation of alerts, and other quantities appropriate for nightly data generation (aka Level 1 Data Products). The Level 1 photometric calibration is not discussed here.

Section 2 reviews the survey requirements for photometric calibration, while Section 3 describes the foundation of LSST’s calibration procedure, first motivating this procedure by describing the transmission of flux through the atmosphere and LSST system and then from the calibration point of view, trying to recreate the flux from the ADUs measured by the detector. Sections ?? and 5 describe those aspects in some detail. Section 6 describes how the LSST’s internal photometric scale is tied to external references. Section 7 describes the hardware required to realize the calibration process. Section 8 presents the error budget for each step of the calibration procedure. Section 9 describes how we will verify that the calibration system functions as designed, and meets the science requirements, first during the construction phase, and later during survey operations. Section 10 describes the implementation of the calibration process in software that will be part of LSST Data Management. Finally, Section 11 discusses the risks that remain in the implementation of the calibration process, and the steps we are taking to mitigate them.

2. Photometric Requirements

The LSST Science Requirements Document (SRD) provides a set of requirements on the annual Data Release (Level 2) photometry. These requirements are extended in the XXX (OSS) to cover aspects which are too detailed for the SRD. based on measurements of bright, unresolved, isolated, non-variable objects from individual LSST visits. **TODO - address what these requirements actually apply to. MS stars vs other SEDs and reference App C. Also be explicit that calibration is based on objects with well-known SEDs - i.e. MS stars.** Bright implies that the measurement of the star’s brightness is not dominated by photon statistics, approximately 1-4 magnitudes fainter than the saturation limit in a given filter. Isolated implies that the star can be successfully de-blended from background galaxies and other stars. Non-variable objects are intrinsically not variable; these will be identified in an iterative fashion from the many epochs of LSST observations. The SRD specifications are:

1. **Repeatability:** the median value of the photometric scatter for each star (the rms of calibrated magnitude measurements around the mean calibrated magnitude) shall not exceed 5 millimags in *gri*, 7.5 millimags in *uzy* for bright, unresolved, isolated, non-variable objects. No more than 10% of these objects should have a photometric scatter larger than 15 mmag in *gri*, 22.5 mmag in *uzy*. This specifies the distribution of photometric errors (σ) and constrains both the repeatability of extracting counts from images and the ability to monitor (or model) the changes in the system response. It could be thought of as requiring the photometry of a single source to be consistent over time.
2. **Uniformity:** the rms of the internal photometric zeropoint error (for each visit) shall not exceed 10 millimags in *grizy*, 20 millimags in *uzy*, where the zeropoint for each visit is determined using bright, unresolved, isolated, non-variable sources. No more than 10% of these sources should be more than 15 mmag in *gri* or 22.5 mmag in *uzy* from the mean internal zeropoint. This places a constraint on the stability of the photometric system across the sky as well as an upper limit on various systematic errors, such as any correlation of photometric calibration with varying stellar populations (or colors). This makes the photometry of many sources comparable over the entire sky, and when combined with the previous requirement, creates a stable photometric system across the sky and over time, in a single filter.
3. **Band-to-band photometric calibration:** The absolute band-to-band zeropoint calibration for main sequence stars must be known with an rms accuracy of 5 millimags for any color not involving *u* band, 10 millimags for colors constructed with *u* band photometry. This places an upper limit on the systematic error in the measurement of the system throughput as a function of wavelength. This requirement ties photometric measurements in different filters together, enabling precise measurement of colors.
4. **Absolute photometric calibration:** The LSST photometric system must transform to an external physical scale (*e.g.* AB mags) with an rms accuracy of 10 millimags. This requirement not only ties LSST internal photometry to photometry obtained from other telescopes, using other photometric systems, but also ties LSST internal photometry to a real physical scale. This places a constraint on the upper limit of the systematic error in the measurement of the total system throughput. This final step enables LSST photometry to be compared directly to data from other telescopes or to models (*e.g.* such as determining the albedo of an asteroid with a known diameter).

Requirements 1 and 2 must be met by measuring and then correcting for changes in hardware and atmospheric transmission as a function of time, location in the sky or focal

plane, and result in a relative calibration within a single filter. Requirements 3 and 4 require comparison of LSST measurements to externally calibrated spectrophotometric standards, providing a relative calibration from filter to filter as well as an absolute physical scale for the overall system. Performance of the LSST system regarding requirement 1 can be verified by simply measuring the rms of the calibrated magnitude measurements. Verification of requirement 2 is more complicated; in a simulated system it is simple to compare the (simulated, thus known) true magnitudes of the stars to the best-fit magnitudes produced after calibration. **TODO forward reference new section on verification - Tim to write** In operations, this will be verified using a combination of simulations, comparisons to known standards, and evaluation of science outputs such as stellar locus diagrams. These last two tests are also relevant to verifying the final two requirements, 3 and 4.

TODO - Lynne (or someone) to verify consistency with new SRD reqs, *after* updating rest of doc and seeing effect of including new SEDs in SRD requirements. Plus need update of SRD to verify.

3. The Photometric Calibration Process

In traditional photometric calibration, a set of standard stars are observed at a range of airmasses to calculate zeropoint offsets and (typically) a single color-dependent extinction curve per night. With care, this approach can deliver 1% photometry in stable photometric conditions. Such programs typically follow only a few objects, and devote roughly equal time to standards and program objects. This approach fails for a survey like LSST, for at least two reasons. First, from a calibration point of view, the very wide field and multiple detector array mean that effectively a large number of instruments must be calibrated rather than just one. Second, historical weather data from Cerro Pachón tells us only 53% of the available observing time can be considered photometric even at the 1–2% level. To take advantage of the full 85% of the available observing time which is usable (total cloud extinction less than 1.5 magnitudes), and to reach the SRD specified requirements – 0.5% level photometric repeatability and 1% photometric uniformity – requires a new approach.

This new approach, variants of which are already in use at PanSTARRS and DES, *directly* measures the system throughput as a function of wavelength, focal plane position, and time. Further, the *normalization* of the throughput in each observation (the gray-scale zeropoint) and the *shape* of the throughput curve (the color dependent terms), are explicitly separated and measured with separate procedures for both the telescope system response and the atmospheric transmission. This calibration system requires various pieces of hardware to conduct these optimized measurements. We briefly describe them here, with full descriptions

in Section 7:

- A dome screen projector designed to provide uniform ($\sim 10\%$ variation) illumination across the field of view, while minimizing stray light. This projector system will have the capability to not only illuminate the screen with broadband white light, but also narrow-band light to measure the system response at individual wavelengths. The narrow-band light will be generated by a tunable laser, capable of producing light from 300 – 1100 nm and tunable in 1 nm increments. The brightness of the screen is measured with a NIST-calibrated photodiode, so that the relative intensity at different wavelengths is precisely determined.
- A 1.2-m auxiliary telescope with an $R \approx 400$ spectrograph, located adjacent to the LSST itself. This auxiliary telescope will obtain spectra of a chosen set of atmospheric probe stars across the sky to determine an atmospheric absorption model.
- Water vapor monitoring system, consisting of a GPS system and a microwave radiometer attached copointed with the LSST telescope, and monitoring the same field of view. This supplements the auxiliary telescope spectra, which are unable to track the sometimes rapid variations of water vapor in time and space.

An overview of the entire calibration process, from science observation to calibrated photometric measurements, together with the required calibration data products is shown in Figures 1, 2, 3, and 4. Note that four classes of objects participate in the calibration process in different ways:

- Standard stars. These are stars whose absolute flux as a function of wavelength above the atmosphere is precisely known. This class contains only a few members, perhaps as few as ten. Their role is to enable the self calibration process to set absolute zeropoints for each band, and to allow testing of the SRD uniformity requirements. See Section 6.
- Calibration stars. These are stars that densely cover the sky, with typical spacings between stars of order 1 arcminute. Unlike standard stars, neither their SEDs nor their absolute fluxes are precisely known, and their standard magnitudes are determined by the self calibration process. They have been selected to be on the stellar main sequence, to be nonvariable, and to be relatively isolated so that their photometry is not degraded by crowding effects.
- Atmospheric probe stars. These are bright stars of known type, distributed roughly uniformly over the LSST sky, which yield high SNR spectra from the auxiliary telescope.

- Science objects. Calibration of science objects utilizes the results of processing the standards and the calibration stars, and the measurement of the system bandpass. If an SED is supplied for an object, an accurate standard magnitude can then be calculated.

The following section will provide a more in-depth overview of the calibration process. We will start with a review of what is physically happening to photons in their path toward the focal plane, and then outline how LSST will translate the measured ADU counts back to fluxes above the atmosphere.

We find it helpful to define four different magnitudes, and their associated fluxes:

- m_b^{inst} , the instrumental magnitude. $m_b^{inst} = -2.5 \log_{10}(C_b^{obs})$, where C_b^{obs} are the instrumental counts (ADU) that are attributed to the object
- m_b^{nat} , the natural magnitude. This is the magnitude in the AB system that would be measured for the object if it were measured through the actual normalized system bandpass, $\phi_b^{obs}(\lambda)$, at the top of the atmosphere. This bandpass varies from exposure to exposure. See equations 7 and 9. $m_b^{nat} = m_b^{inst} + Z_b^{obs}$
- m_b^{std} , the standard magnitude. This is the magnitude in the AB system that would be measured for the object if it were measured through the standard normalized system bandpass, $\phi_b^{std}(\lambda)$, at the top of the atmosphere. This bandpass is selected as part of the survey design, and does not vary. See equation 8.
- m_b^{corr} , the SED corrected instrumental magnitude. This is the standard magnitude, but with an unknown gray zeropoint correction, which will be removed by self calibration. These magnitudes are the input to self calibration. $m_b^{corr} = m_b^{inst} + \Delta m_b^{obs}$

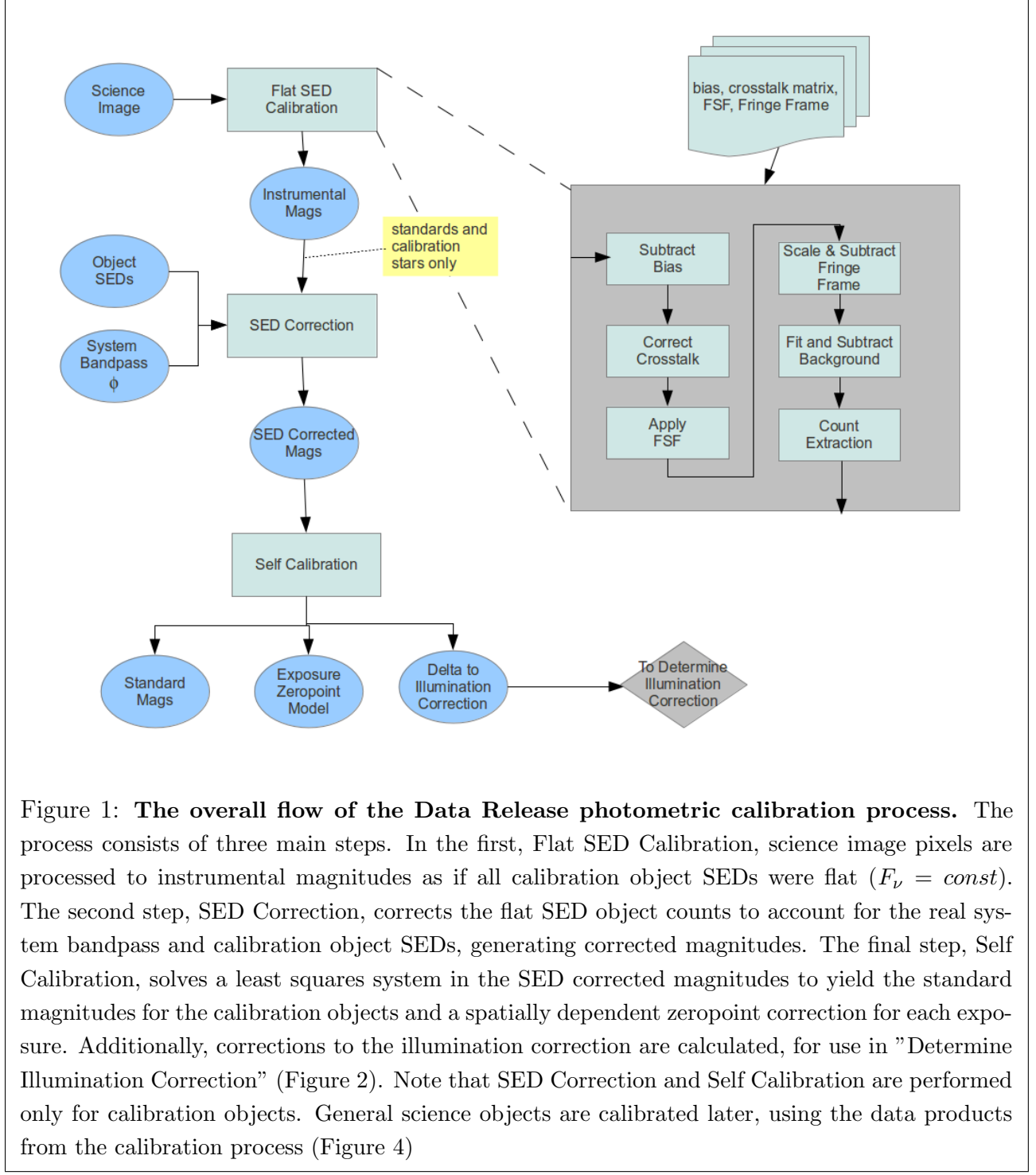
These quantities are related through equations 15 and 15.

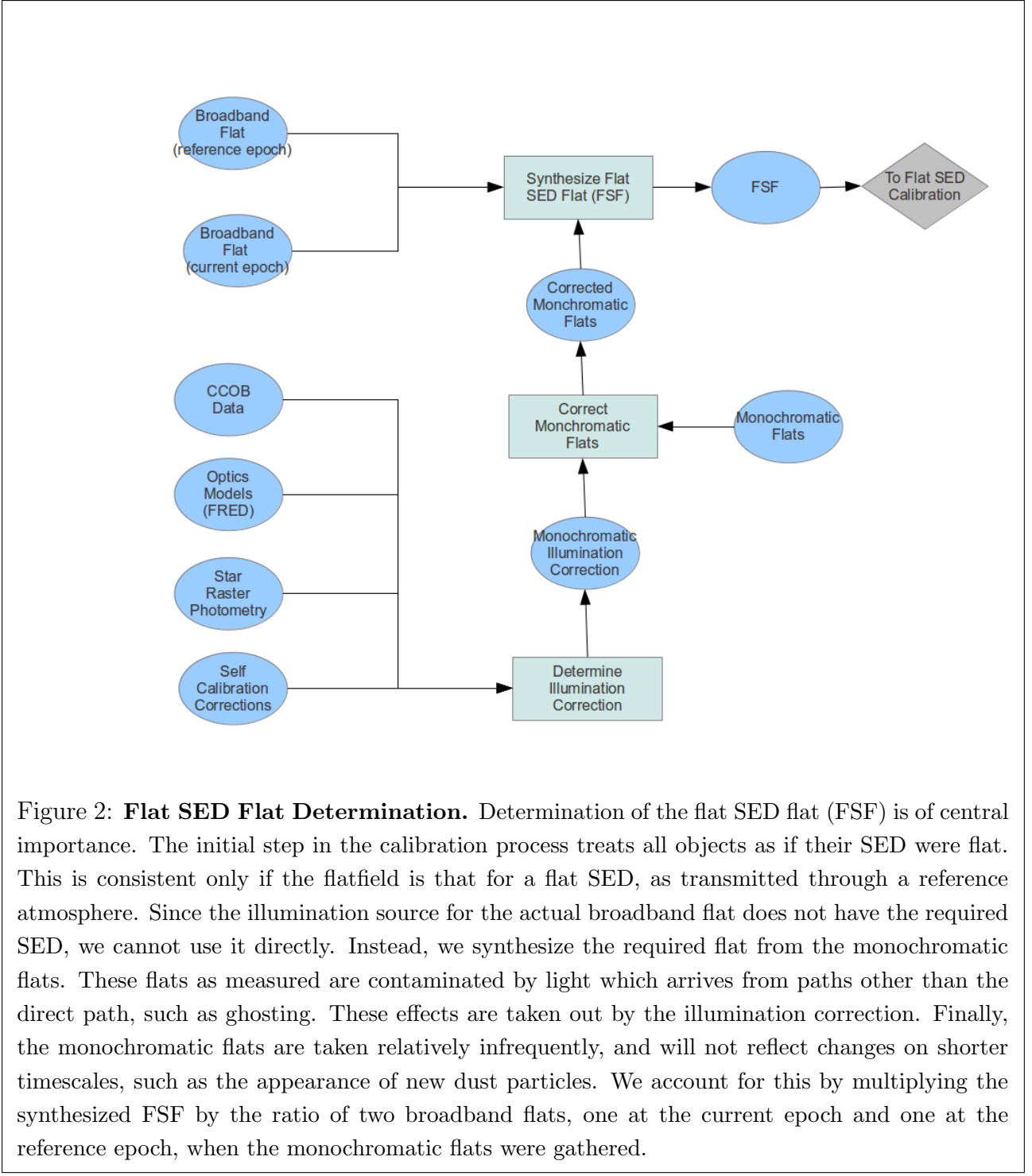
4. From Flux to Counts

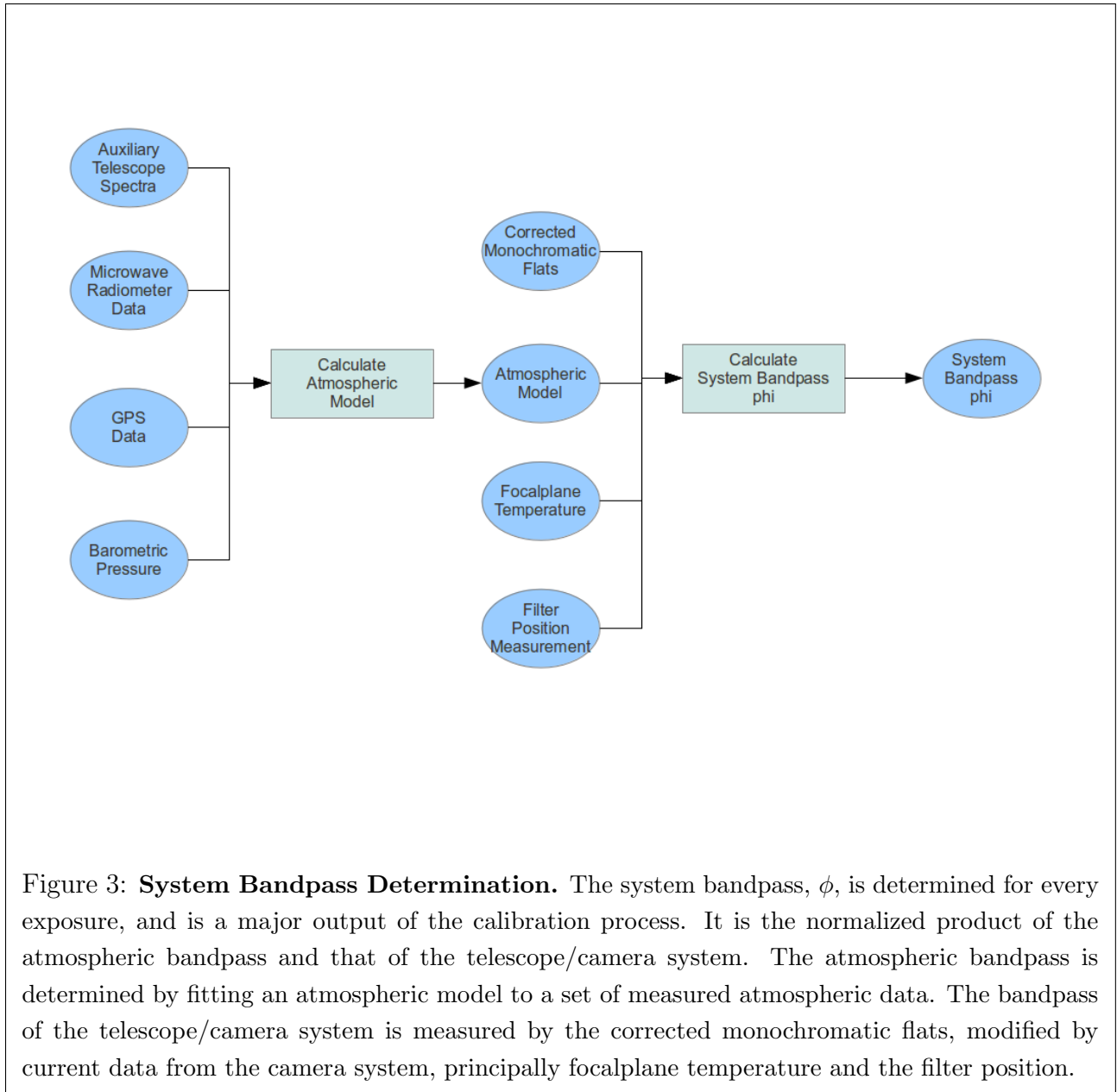
We first consider how the photons from an astronomical object make their way to the detector and are converted into counts (ADUs), paying attention to the various temporal or spatial scales for variability might arise in the LSST system to affect the final ADU counts.

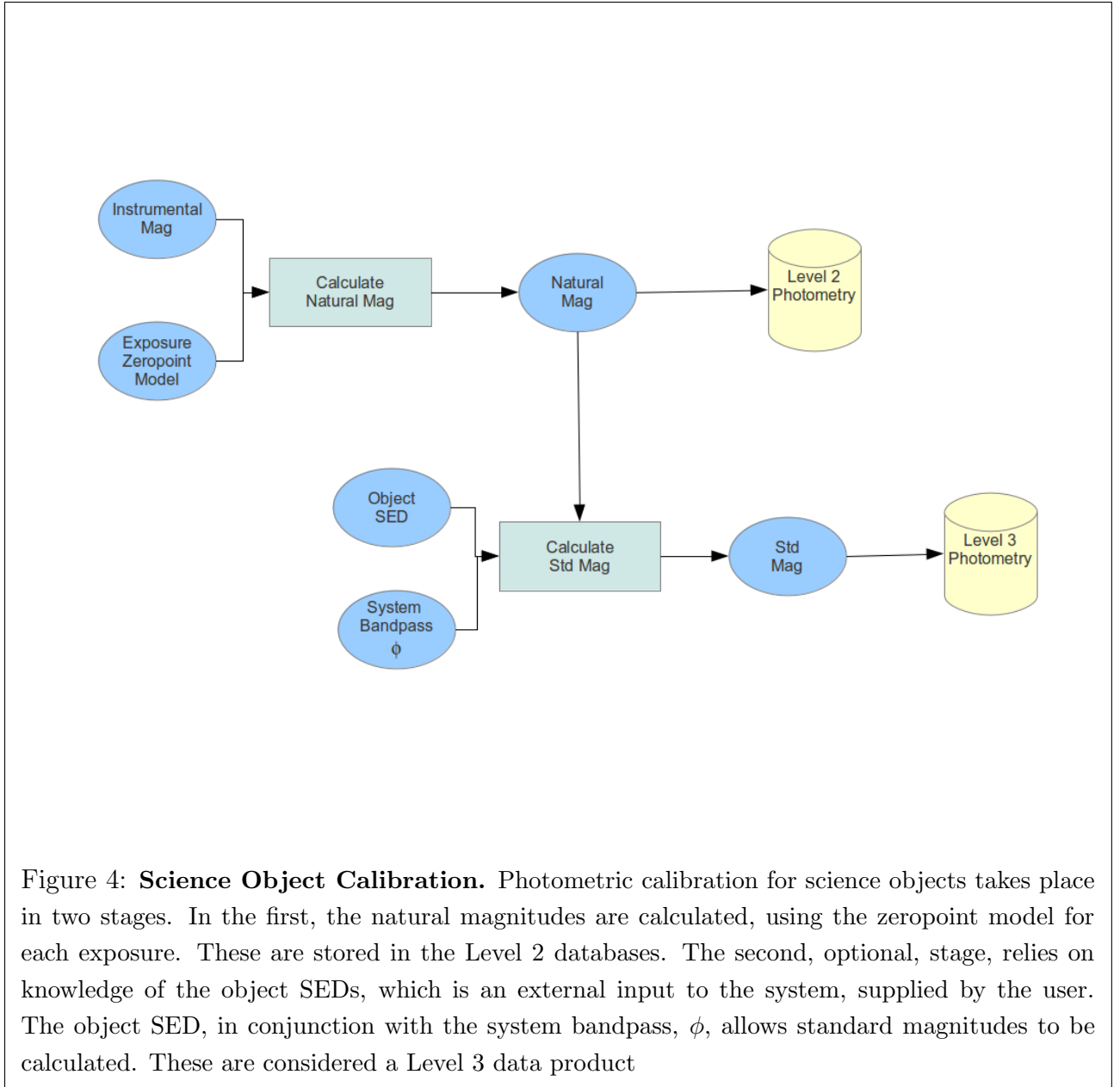
Given $F_\nu(\lambda, t)$ – the specific flux¹ (flux per unit frequency) of an astronomical object

¹Hereafter, the units for specific flux (flux per unit are Jansky (1 Jy = 10^{-23} erg cm $^{-2}$ s $^{-1}$ Hz $^{-1}$). The









at the top of the atmosphere – at a position described by (alt, az) , the total flux from the object transmitted through the atmosphere to the telescope pupil is

$$F_\nu^{pupil}(\lambda, alt, az, t) = F_\nu(\lambda, t) S^{atm}(\lambda, alt, az, t), \quad (1)$$

where $S^{atm}(\lambda, alt, az)$ is the (dimensionless) probability that a photon of wavelength λ makes it through the atmosphere,

$$S^{atm}(\lambda, alt, az, t) = e^{-\tau^{atm}(\lambda, alt, az, t)}. \quad (2)$$

Here $\tau^{atm}(\lambda, alt, az)$ is the optical depth of the atmospheric layer at wavelength λ towards the position (alt, az) . Observational data (Stubbs et al. 2007; Burke et al. 2010) show that the various atmospheric components which contribute to absorption (water vapor, aerosol scattering, Rayleigh scattering and molecular absorption) can lead to variations in $S^{atm}(\lambda, t)$ on the order of 10% per hour. Clouds represent an additional gray (non-wavelength dependent) contribution to τ^{atm} that can vary even more rapidly, on the order of 2–10% of the total extinction at 1° scales within minutes (Ivezić et al. 2007).

Given the above $F_\nu^{pupil}(\lambda, alt, az, t)$, the total ADU counts transmitted from the object to a footprint within the field of view at (x, y) can be written as

$$C_b(alt, az, x, y, t) = C \int_0^\infty F_\nu^{pupil}(\lambda, alt, az, t) S_b^{sys}(\lambda, x, y, t) \lambda^{-1} d\lambda. \quad (3)$$

Here, $S_b^{sys}(\lambda, x, y, t)$ is the (dimensionless) probability that a photon will pass through the telescope’s optical path to be converted into an ADU count, and includes the mirror reflectivity, lens transmission, filter transmision, and detector sensitivity. The term λ^{-1} comes from the conversion of energy per unit frequency into the number of photons per unit wavelength and b refers to a particular filter, *ugrizy*. The dimensional conversion constant C is

$$C = \frac{\pi D^2 \Delta t}{4gh} \quad (4)$$

where D is the effective primary mirror diameter, Δt is the exposure time, g is the gain of the readout electronics (number of photoelectrons per ADU count, a number greater than one), and h is the Planck constant. The wavelength-dependent variations in S_b^{sys} generally change

choice of F_ν vs. F_λ makes the flux conversion to the AB magnitude scale more transparent, and the choice of λ as the running variable is more convenient than the choice of ν . Note also, while $F_\nu(\lambda, t)$ (and other quantities that are functions of time) could vary more quickly than the standard LSST exposure time of 15s, it is assumed that all such quantities are averaged over that short exposure time, so that t refers to quantities that can vary from exposure to exposure.

quite slowly in time; over periods of months, the mirror reflectance and filter transmission will degrade as their coatings age. A more rapidly time-varying wavelength-dependent change in detector sensitivity (particularly at very red wavelengths in the y band) results from temperature changes in the detector, but only on scales equivalent to a CCD or larger. There will also be wavelength-dependent spatial variations in S_b^{sys} due to irregularities in the filter material; these are required by the camera specifications to vary (at a maximum) slowly from the center of the field of view to the outer edges, equivalent to a bandpass shift on the order of 1-2% of the effective wavelength of the filter. Wavelength-independent (gray-scale) variations in S_b^{sys} can occur more rapidly, on timescales of a day for variations caused by dust particles on the filter or dewar window, and on spatial scales ranging from the amplifier level, arising from gain changes between amplifiers, down to the pixel level, in the case of pixel-to-pixel detector sensitivity variations.

From equation 3 and the paragraphs above, we can see that the generation of counts $C_b(alt, az, x, y, t)$ from photons is imprinted with many different effects, each with different variability scales over time, space, and wavelength. In particular the wavelength-dependent variability (bandpass shape) is typically much slower in time and space than the gray-scale variations (bandpass normalization). These different scales of variability motivate us to separate the measurement of the normalization of S_b^{sys} and S^{atm} from the measurement of the wavelength-dependent shape of the bandpass.

4.1. Normalized bandpass response, $\phi_b(\lambda)$

This then leads us to introduce a ‘normalized bandpass response function’, $\phi_b^{obs}(\lambda, t)$, that represents the true bandpass response shape for each observation,

$$\phi_b^{obs}(\lambda, t) = \frac{S^{atm}(\lambda, alt, az, t) S_b^{sys}(\lambda, x, y, t) \lambda^{-1}}{\int_0^\infty S^{atm}(\lambda, alt, az, t) S_b^{sys}(\lambda, x, y, t) \lambda^{-1} d\lambda}. \quad (5)$$

Note that ϕ_b only represents *shape* information about the bandpass, as by definition

$$\int_0^\infty \phi_b(\lambda) d\lambda = 1. \quad (6)$$

Using $\phi_b^{obs}(\lambda, t)$ we can represent the (true, total) in-band flux of an object for each observation as

$$F_b^{obs}(t) = \int_0^\infty F_\nu(\lambda, t) \phi_b^{obs}(\lambda, t) d\lambda, \quad (7)$$

where the normalization of $F_b(t)$ corresponds to the top of the atmosphere. Unless $F_\nu(\lambda, t)$ is a flat ($F_\nu(\lambda) = \text{constant}$) SED, F_b^{obs} will vary with changes in $\phi_b^{obs}(\lambda, t)$ due simply to

changes in the bandpass shape, such as changes with position in the focal plane or differing atmospheric absorption characteristics, *even if the source is non-variable*.

To provide a reported $F_b^{std}(t)$ which is constant for non-variable sources, we also introduce the ‘standardized bandpass response function’, $\phi_b^{std}(\lambda)$, a curve that will be defined before the start of LSST operations (most likely during commissioning). $\phi_b^{std}(\lambda)$ represents a typical hardware and atmospheric transmission curve, minimizing the difference between $\phi_b^{obs}(\lambda, t)$ and the standardized reported bandpass. Now,

$$F_b^{std}(t) = \int_0^\infty F_\nu(\lambda, t) \phi_b^{std}(\lambda) d\lambda, \quad (8)$$

is a constant value for non-variable sources.

Magnitudes provide an easy way to conceptualize the relationship between F_b^{obs} and F_b^{std} , provided that we define a ‘natural magnitude’

$$m_b^{nat} = -2.5 \log_{10} \left(\frac{F_b^{obs}}{F_{AB}} \right) \quad (9)$$

where $F_{AB} = 3631$ Jy. The natural magnitude, like F_b^{obs} will vary from observation to observation as $\phi_b^{obs}(\lambda, t)$ changes, even if the source itself is non-variable. The natural magnitude can be translated to a ‘standard magnitude’, m_b^{std} , as follows:

$$m_b^{nat} = -2.5 \log_{10} \left(\frac{F_b^{obs}}{F_{AB}} \right) \quad (10)$$

$$= -2.5 \log_{10} \left(\frac{\int_0^\infty F_\nu(\lambda, t) \phi_b^{obs}(\lambda, t) d\lambda}{F_{AB}} \right) \quad (11)$$

$$= -2.5 \log_{10} \left(\left(\frac{\int_0^\infty F_\nu(\lambda, t) \phi_b^{obs}(\lambda, t) d\lambda}{\int_0^\infty F_\nu(\lambda, t) \phi_b^{std}(\lambda, t) d\lambda} \right) \left(\frac{\int_0^\infty F_\nu(\lambda, t) \phi_b^{std}(\lambda, t) d\lambda}{F_{AB}} \right) \right) \quad (12)$$

$$m_b^{nat} = \Delta m_b^{obs} + m_b^{std} \quad (13)$$

$$\Delta m_b^{obs} = -2.5 \log_{10} \left(\frac{\int_0^\infty F_\nu(\lambda, t) \phi_b^{obs}(\lambda, t) d\lambda}{\int_0^\infty F_\nu(\lambda, t) \phi_b^{std}(\lambda, t) d\lambda} \right) \quad (14)$$

where Δm_b^{obs} varies with the *shape* of the source spectrum, $f_\nu(\lambda, t)$ and the *shape* of the bandpass $\phi_b^{obs}(\lambda, t)$ in each observation. Note that $\Delta m_b^{obs} = 0$ for flat (constant) SEDs, as the integral of $\phi_b(\lambda)$ is always one. For non-variable sources, m_b^{std} will be non-variable as it represents the throughput in a standardized bandpass, $\phi_b^{std}(\lambda)$.

The natural and standard magnitudes can be tied back to the counts produced by the system by adding the correct zeropoint offsets. As Δm_b^{obs} removes all wavelength dependent

variations in m_b^{std} ,

$$m_b^{std} = m_b^{inst} - \Delta m_b^{obs} + Z_b^{obs} \quad (15)$$

$$\equiv m_b^{corr} + Z_b^{obs} \quad (16)$$

where

$$m_b^{inst} = -2.5 \log_{10}(C_b^{obs}) \quad (17)$$

The zeropoint correction here, Z_b^{obs} , contains only gray-scale *normalization* effects, such as variations due to the flat field or cloud extinction. The SED corrected magnitude, m_b^{corr} , is the input to the Self Calibration block in Figure 1.

4.2. Perturbations to the System Bandpass

The normalized system bandpass will vary from exposure to exposure due to a myriad of effects. The major ones are:

- Atmospheric transmission variations. The major wavelength-dependent sources of atmospheric absorption, Rayleigh scattering from molecules, molecular oxygen lines, ozone, water vapor, and aerosols, all vary in time and space, with widely varying temporal and spatial scales. Even in the absence of intrinsic variation in the atmosphere, of course, the bandpass varies due to changing airmass. This latter effect is compensated for in traditional photometric calibration, but the others are generally ignored
- Long term variations in the throughput of the optical path due to contamination
- Changing detector quantum efficiency, particularly in the y-band, due to varying focal plane temperature
- Shifts in filter position with respect to the system optical axis, due to positioning jitter and gravity sag

It bears repeating that every perturbation in general affects both the zeropoint, through the gray component of the perturbation, and the shape of the system bandpass, through the wavelength-dependent component. The gray component is removed by the self calibration process, while the wavelength-dependent component must be separately characterized and removed (see Figure 1). We are concerned here only about the latter effect, and discuss it for each of the above categories.

4.3. Effects of Atmospheric Variations

The main components of wavelength-dependent atmospheric extinction are Rayleigh scattering from molecules; oxygen molecular lines; water vapor; ozone; and aerosols. Rayleigh scattering and molecular oxygen extinctions are directly proportional to barometric pressure at the surface. As is well known from looking at surface pressure charts, away from weather fronts the pressure varies significantly on timescales of hours or more and spatial scales of hundreds of km. Variations can be much more rapid in the vicinity of fronts. In any case, this component can be compensated for very accurately just by measuring the barometric pressure, and we do not further consider it here. The other components are not so easily measured, and in the case of water vapor and aerosols, can display complex patterns of variability.

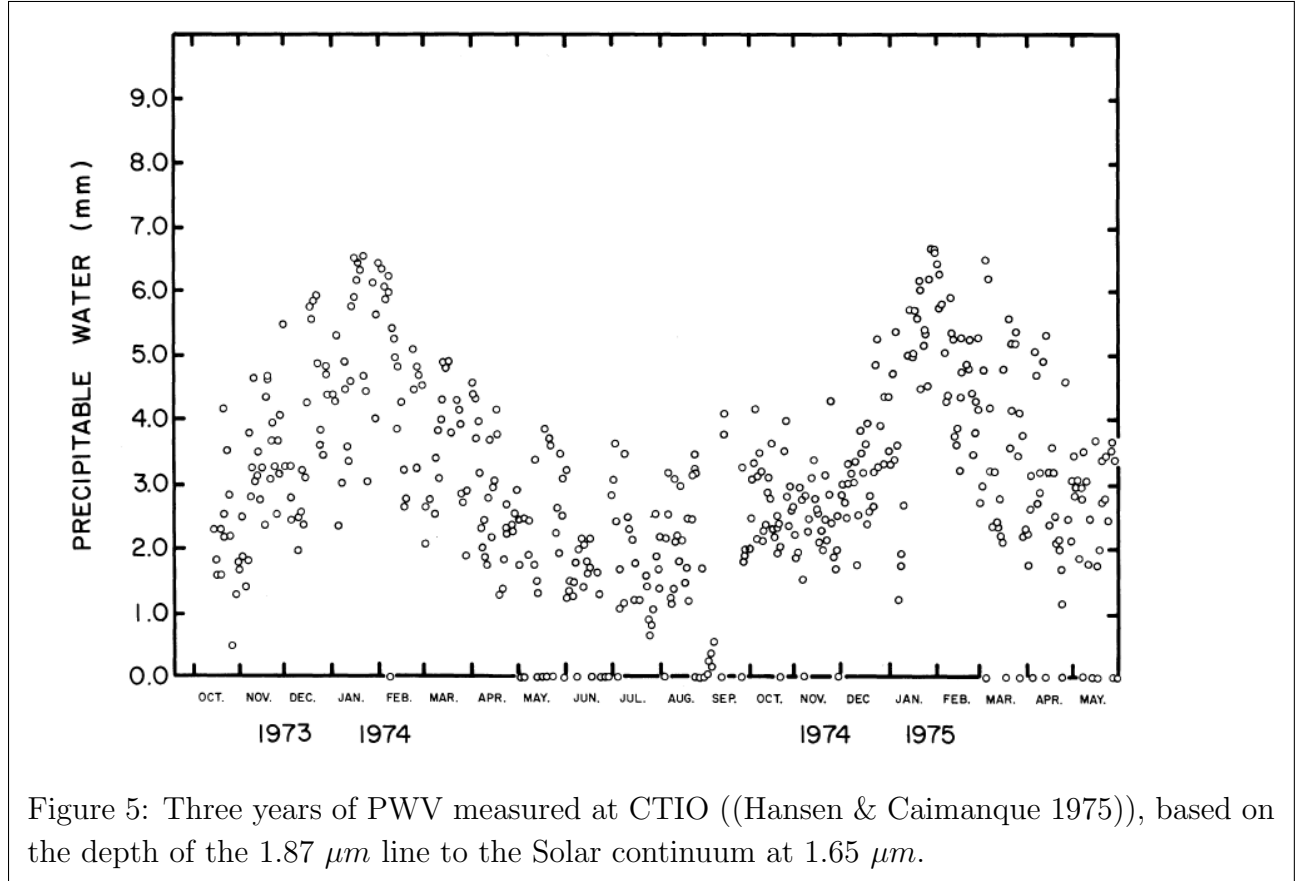
Figures 5, 6, and 7 give three different perspectives on historical water vapor variability in the vicinity of CP. There are broad patterns in space (the E-W gradient), and in time (the regular seasonal variations). There are large variabilities on top of these, amounting to several mm of PWV, which can occur in hours or less. The biggest effect of water vapor is in the y-band, since it contains a strong water band (Figure ??). Figure 8 shows the change in natural magnitude when the PWV is varied from 1mm to 6mm for a set of Kurucz stars. The 4mm variation in PWV shown in Figure 6 would lead to a roughly +/-3mmag color-dependent scatter in calibration of y photometry, if not compensated for.

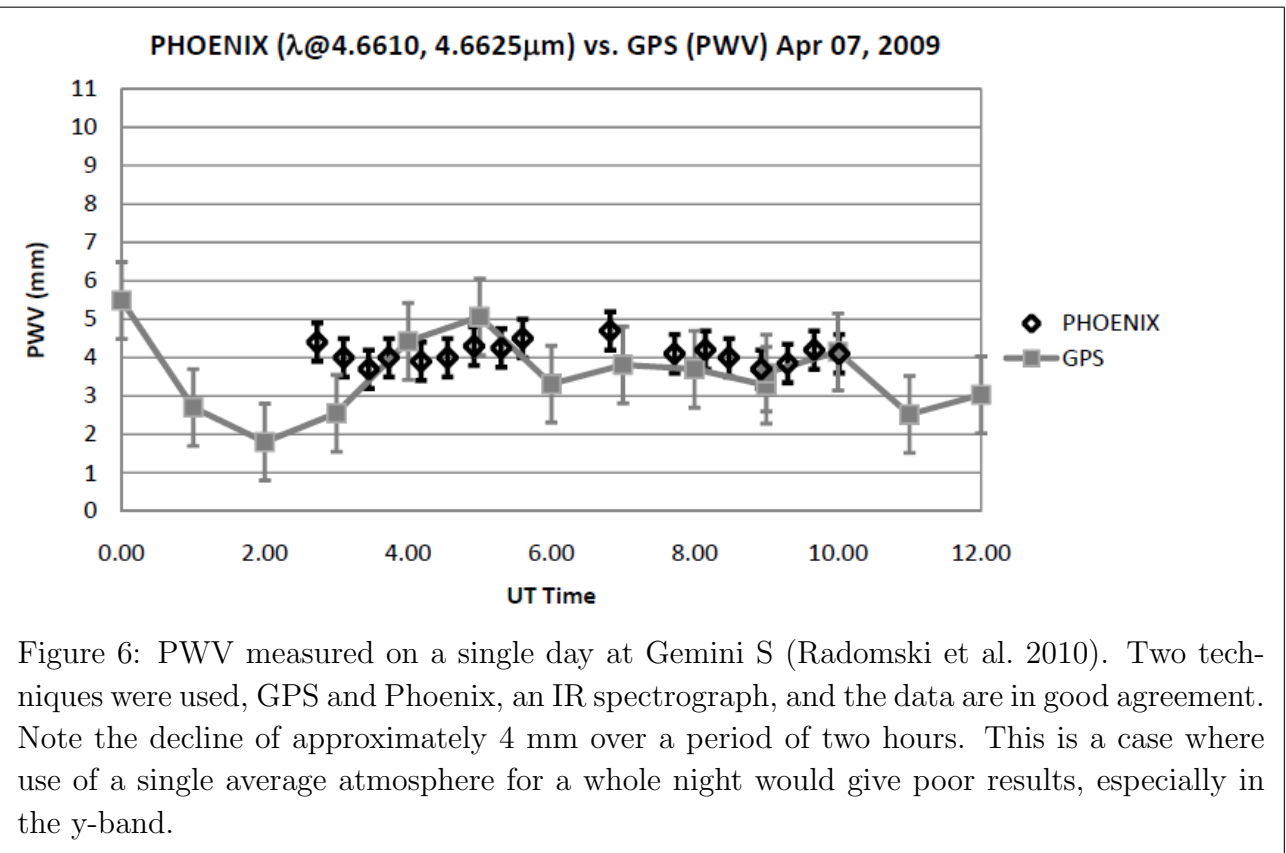
While we do not have aerosol variability data for Cerro Pachon (CP), data from CASLEO, a site at 2550m in Argentina ((?)) serves as a reasonable proxy. Figure 9 shows the time history of aerosol optical depth at 675nm over a period of roughly a year. The spiky nature of the data is notable, suggesting rapid variations on timescales of perhaps a few hours. Figure 10, which shows a time-altitude profile of aerosol variations at a site in the US, backs up this impression. Although the site is at much lower altitude than CP, there are nonetheless significant variation of aerosol extinction at altitudes above 3000m on time scales well under an hour, and we should expect similar variations at CP. Determining the effects of aerosol variations on the system bandpass is more complex than for other atmospheric components, because the spectral shape of the aerosol extinction varies as well as its magnitude. Figure 11 shows the change in natural magnitude when the aerosol optical depth is varied from 0.04 mag to 0.16 mag, roughly the range of the CASLEO data, while keeping a constant spectral index of $\alpha = -1.7$. Unlike water vapor, which affected the reddest bands most strongly, aerosols affect the bluest bands the most. The effects in the u-band range from -5 mmag to +35 mmag, strongly dependent on star color.

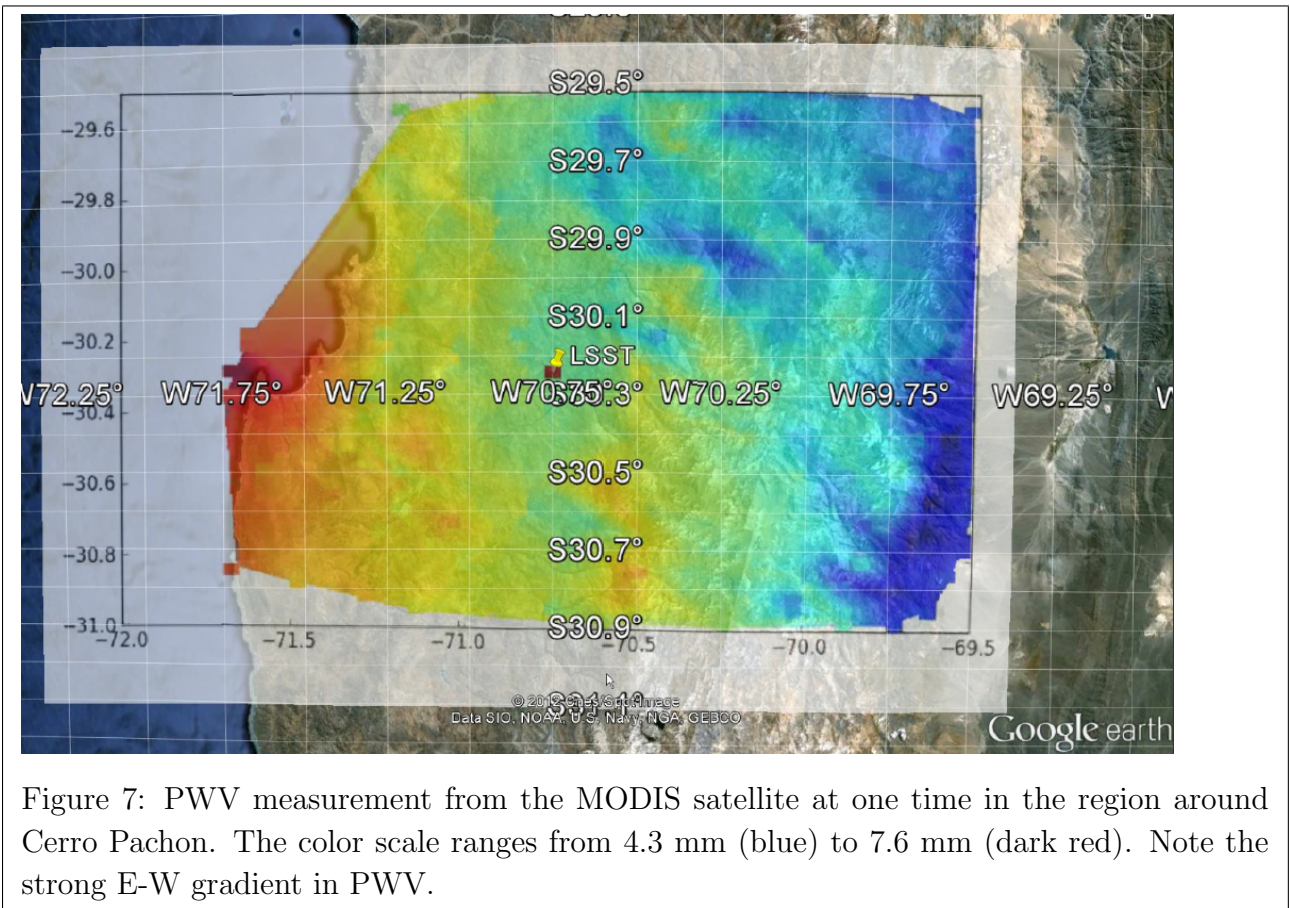
Ozone is dominantly a stratospheric component of the atmosphere, and is routinely monitored by satellite. There is little evidence for variations on short time or space scales,

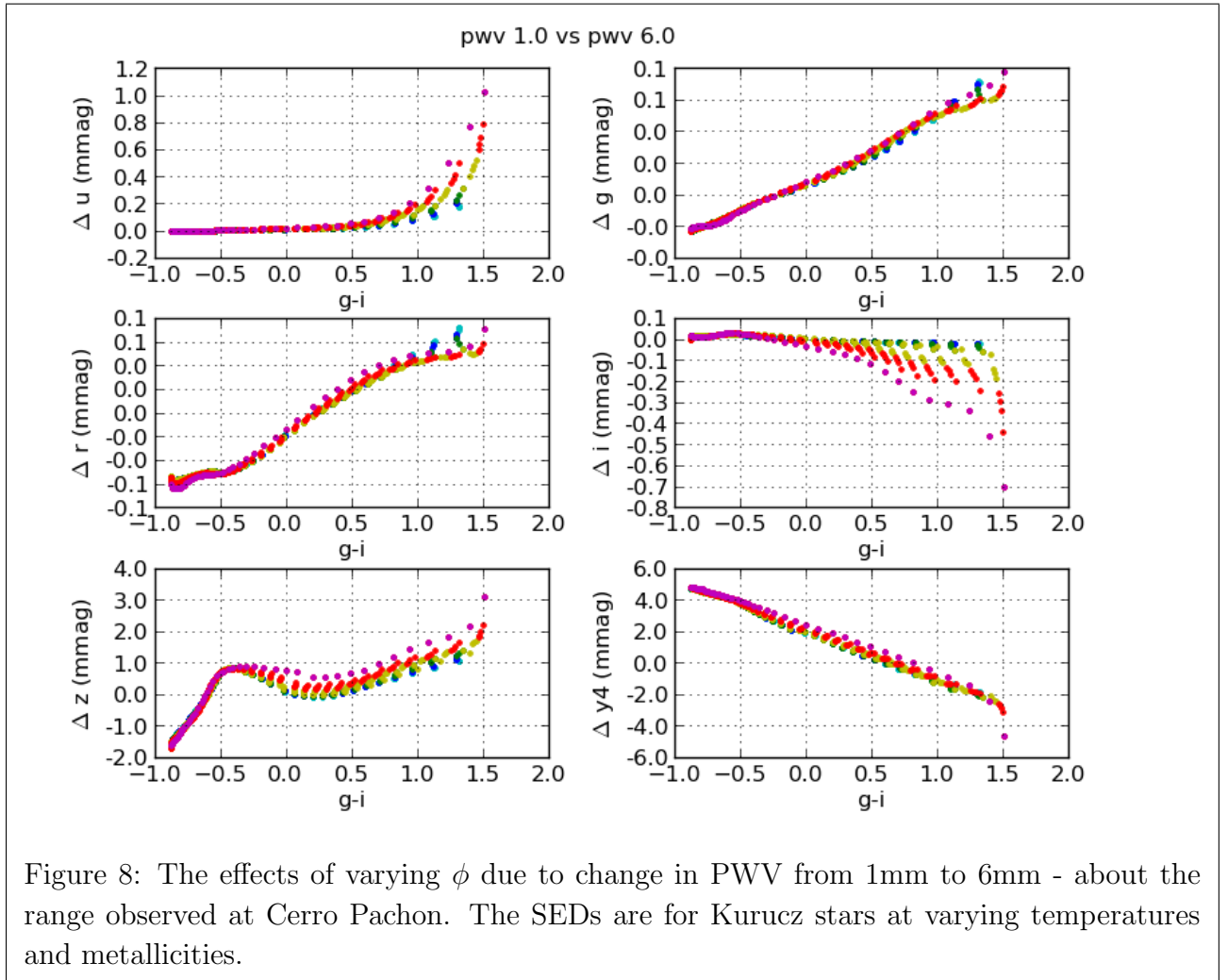
with most variation on a seasonal scale. Figure 12 shows the overall variability of ozone at CP over a roughly 8 year period. Figure 13 shows the changes in the natural magnitudes for a variation in ozone by 50 Dobson units. The effect is very small, except in the u-band, where it has a noticeable effect on red stars.

To summarize the effects of wavelength-dependent atmospheric variations, they are sufficiently large, and occur sufficiently rapidly, that they must be corrected by an atmospheric model with fidelity substantially greater than the traditional photometrist's extinction model. The combination of the auxiliary telescope and the water vapor monitoring system will supply the data required for construction of these atmospheric models. It is also worth emphasizing that correcting for these effects requires not only an accurate bandpass model, but also SEDs for the objects being calibrated. Calibration stars will be picked from well defined stellar populations to minimize SED uncertainty. SED determination for arbitrary science objects, such as supernovae and galaxies, will be more challenging, and may limit the accuracy of their photometric calibration.









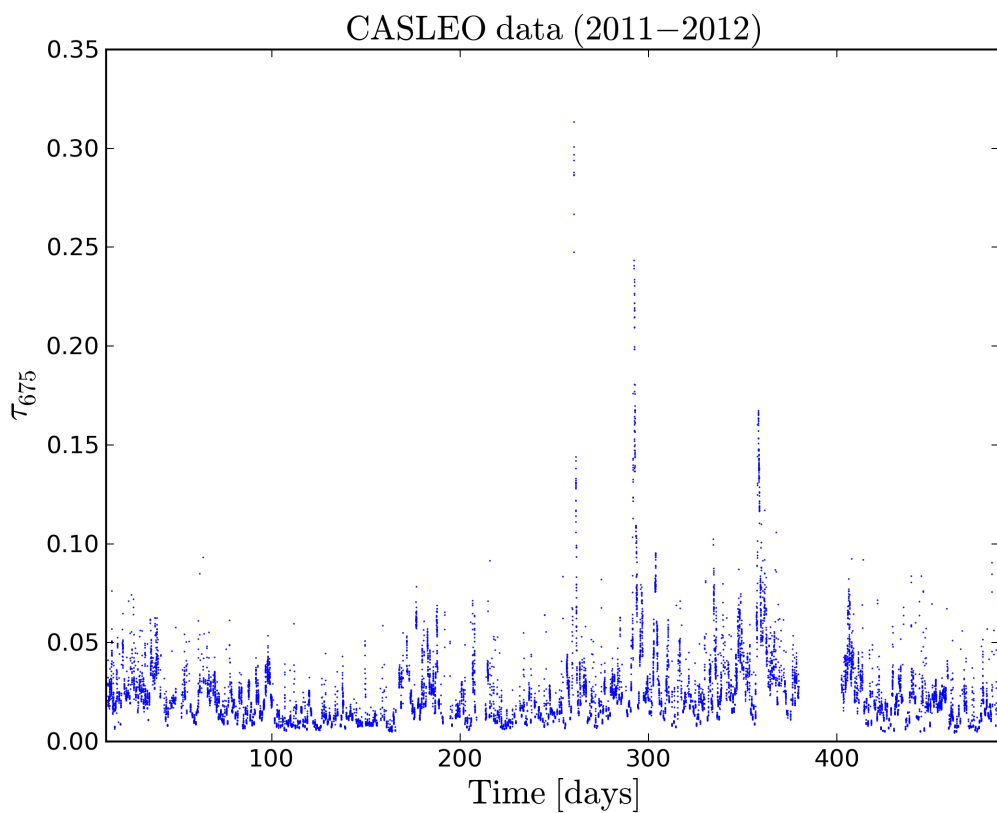


Figure 9: Varying aerosol optical depth at CASLEO, El Leoncito, Argentina. The site elevation at 2550m is similar to CP.

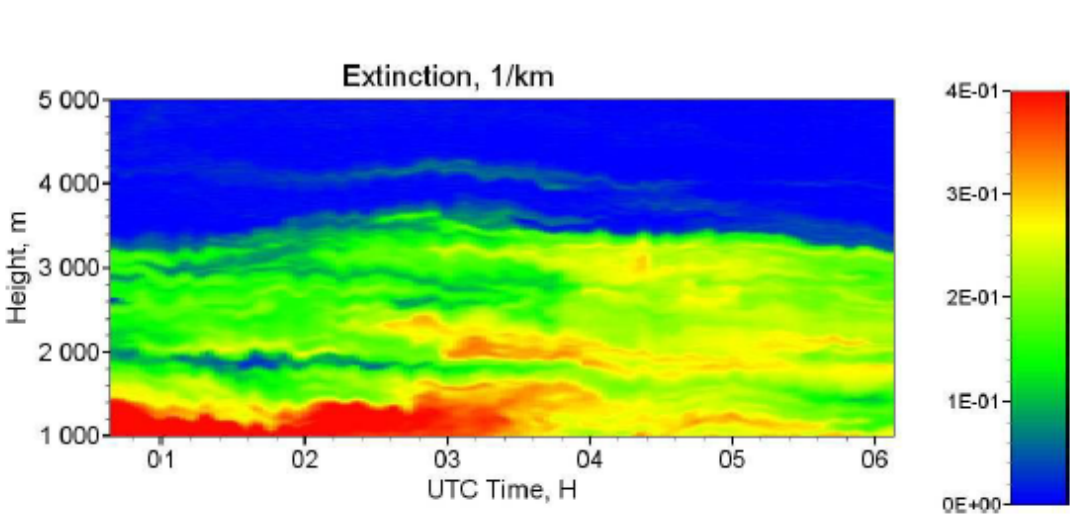


Figure 10: Lidar measurements of aerosol extinction at 355nm over a single night near Greenbelt, MD (Veselovskii et al. 2013). Cerro Pachon is, of course, a different environment, and is at an altitude of 2700m, removing much of the variability. Even above that altitude, however, significant variation on rapid time scales remains.

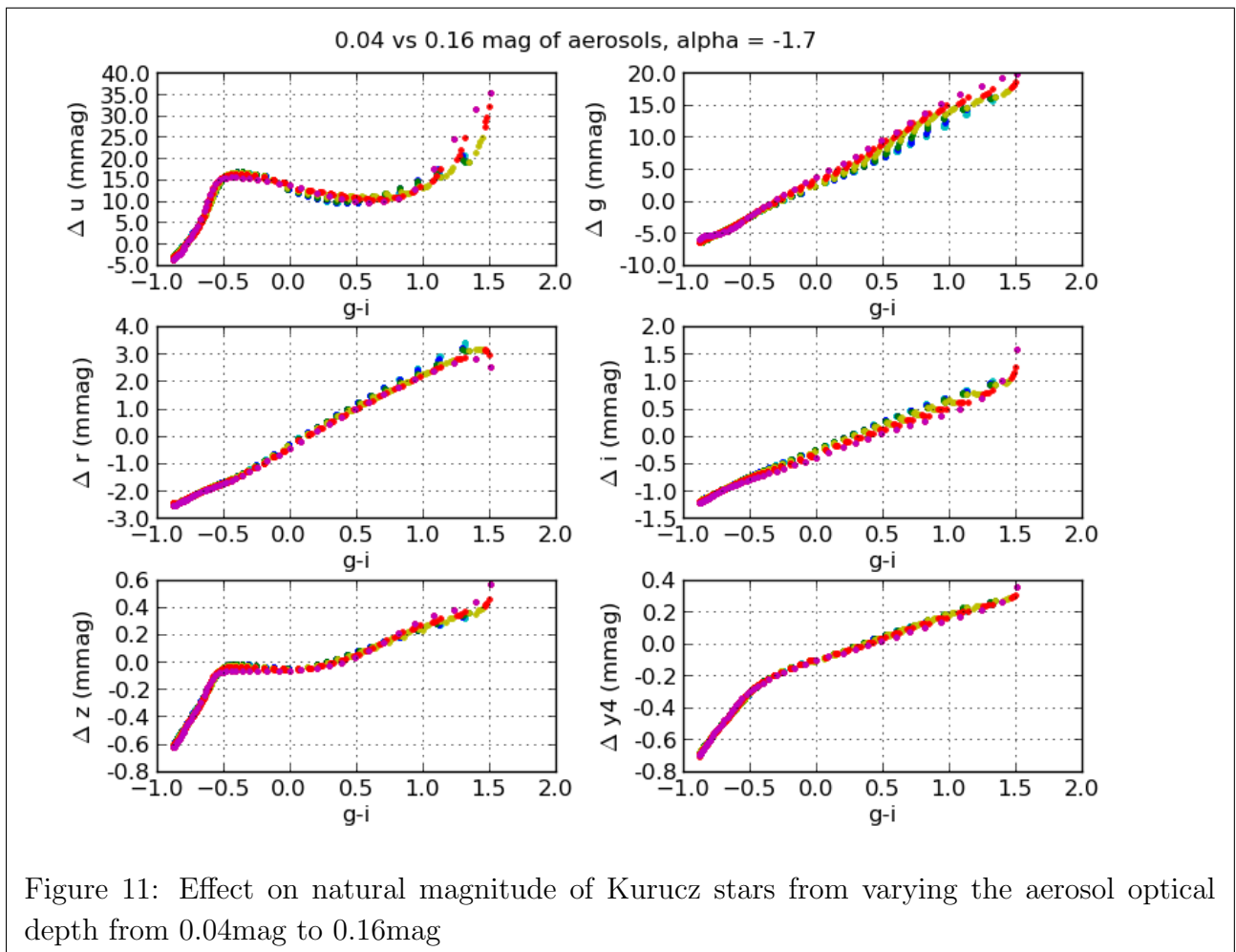
4.4. Throughput Variations Due to Contamination

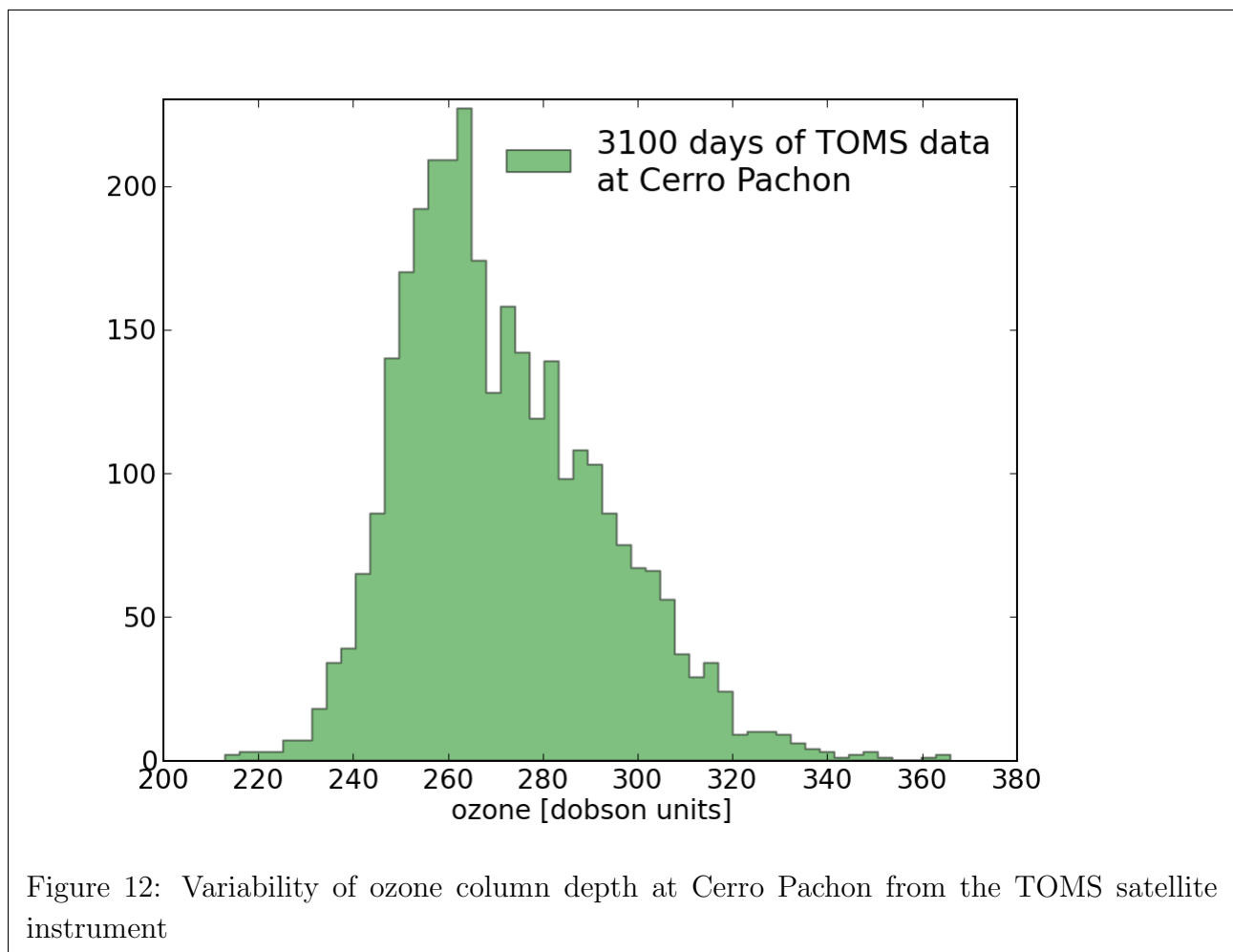
4.5. Variations in Detector Quantum Efficiency

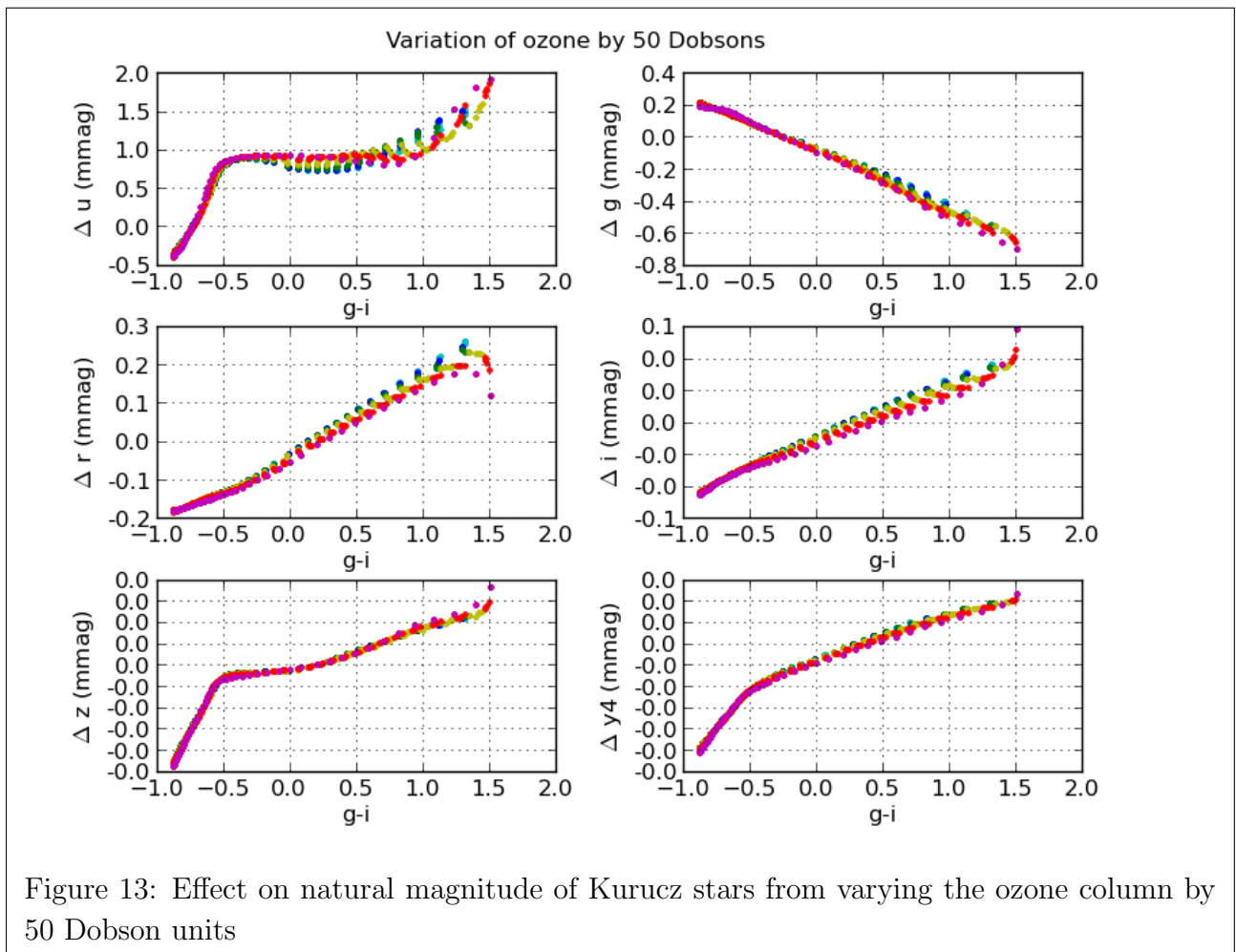
4.6. Throughput Variations Due to Filter Position Shifts

4.7. Putting it All Together

Examples of the Δm_b^{obs} due to variations in the shape of the hardware and atmospheric response curves are shown in Figure 14 and Table 1. Two main sequence stellar models (Kurucz 1993) – one with temperature 35000K (blue) and one 6000K (red) – were combined with three different atmospheric response curves (with airmass $X=1.0$ with minimal H₂O vapor, $X=1.2$ with a nominal amount of H₂O (the ‘standard’), and $X=1.8$ with a large H₂O vapor content) and two different hardware response curves (one ‘standard’ and one shifted in wavelength by 1%) to illustrate the resulting changes in observed natural magnitudes. In Figure 15, the $X = 1.8$ atmospheric response is combined with a 1% shift (the maximum allowed in the filter manufacturing specification from center to edge) in filter bandpass, thus altering the hardware response, for many main sequence Kurucz models spanning a range of $g - i$ colors; the resulting changes in natural magnitudes are plotted. These examples demonstrate that the scatter in natural magnitudes induced by expected atmospheric and







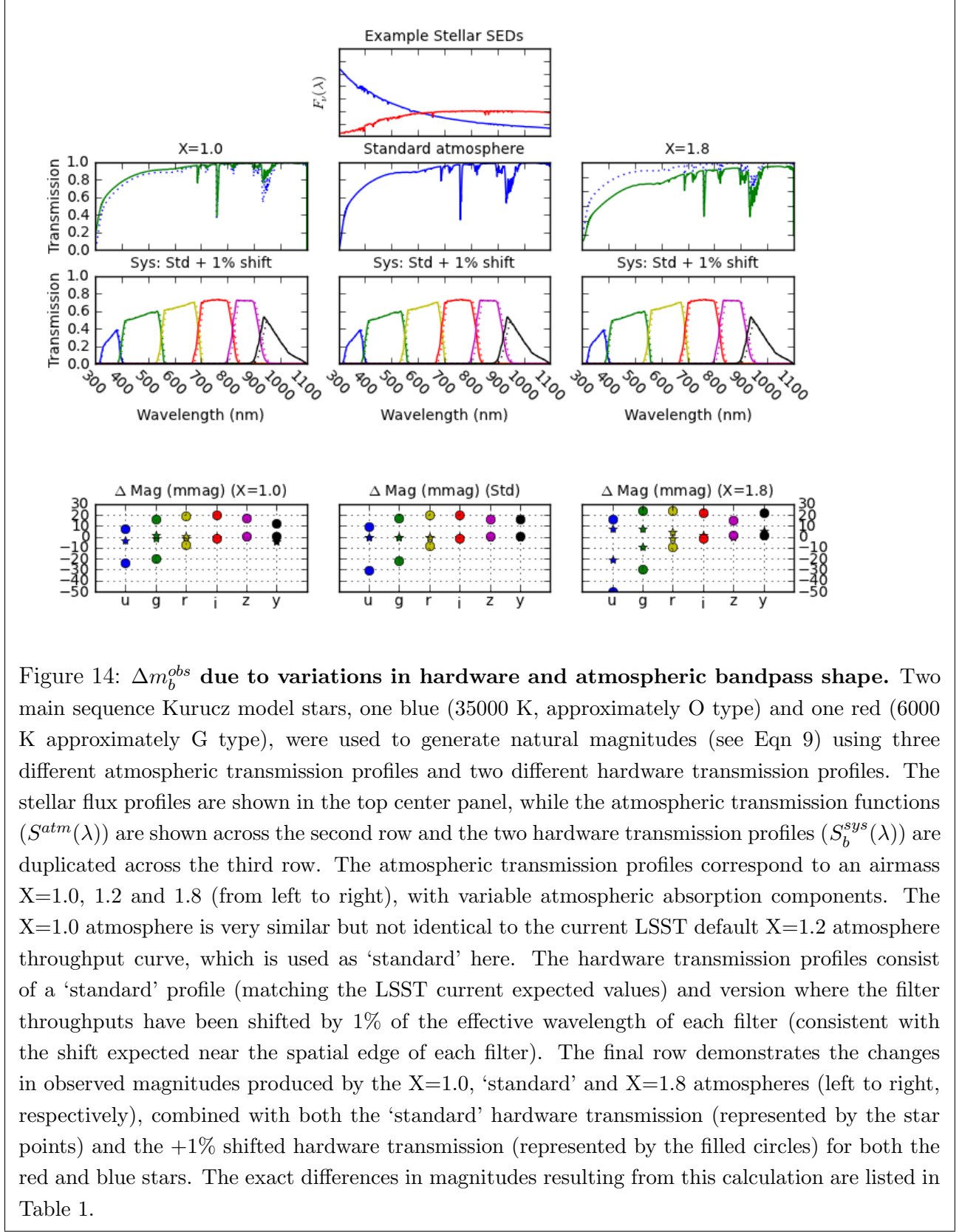
hardware transmission curve shape changes alone (without any gray-scale changes) can be much larger than the SRD repeatability requirements would permit. Roughly speaking, these effects reach a level of about 50 mmag. This suggests that our measurement-based model of wavelength-dependent effects must be accurate at the 90-95% level. This issue is discussed in detail in Section 8

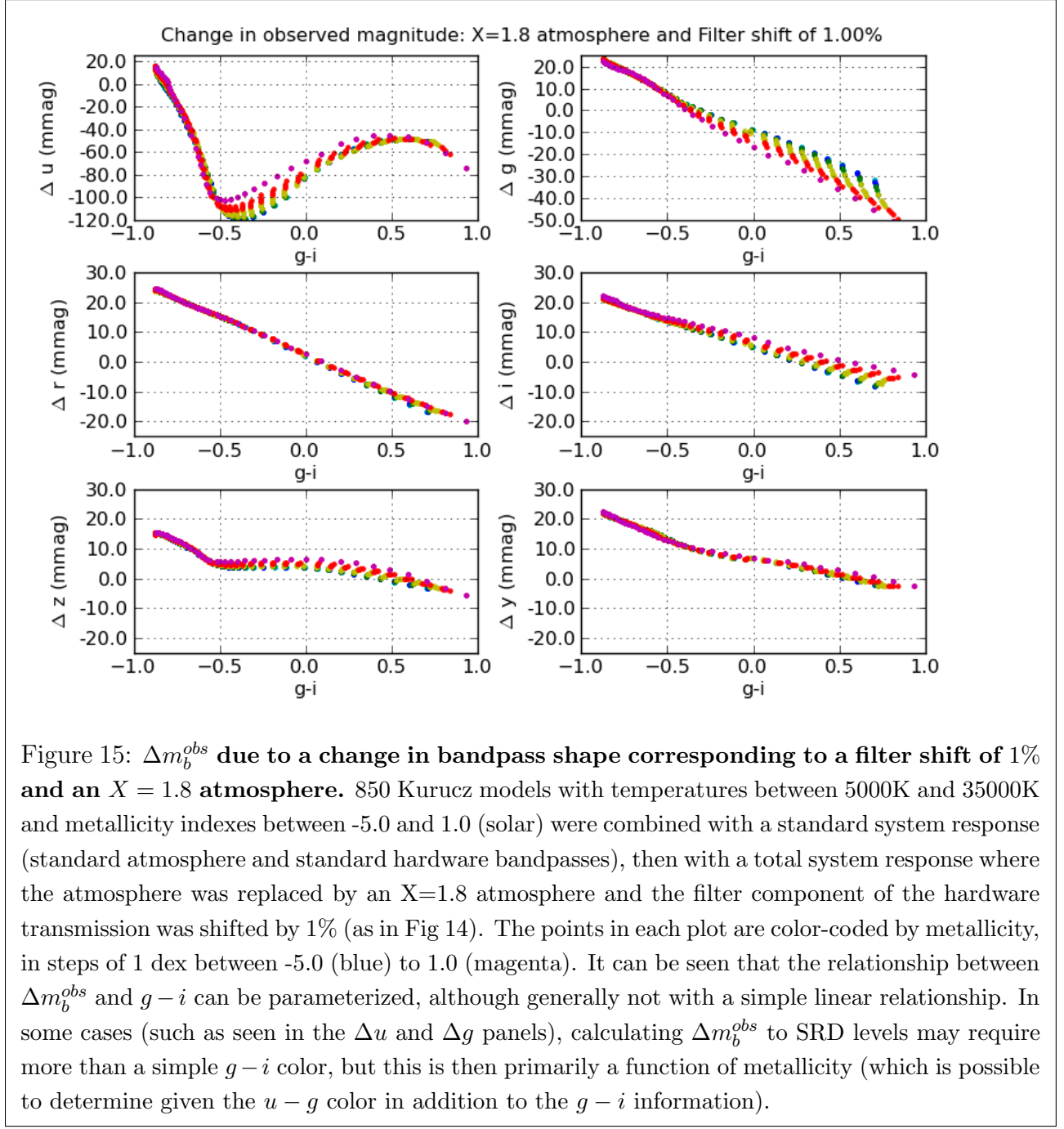
Table 1:: Δm_b^{obs} due to variations in system and atmospheric bandpass shape (see also Fig 14). The first two rows show the baseline ('standard') magnitude of the star. All other rows show the *change* in magnitude (in mmag) due to the variations listed at left. Any value larger than 5 mmag would be larger than the RMS scatter allowed by the SRD. *TODO color-code values larger than 5 mmag*

Bandpass	star	u (mag)	g	r	i	z	y
Std (X=1.2) atm, std sys	red	21.472	20.378	20.000	19.911	19.913	19.913
Std (X=1.2) atm, std sys	blue	19.102	19.503	20.000	20.378	20.672	20.886
		Δu (mmag)	Δg	Δr	Δi	Δz	Δy
Std (X=1.2), +1% sys shift	red	-31	-22	-8	-2	1	1
Std (X=1.2), +1% sys shift	blue	9	17	20	20	16	16
X=1.0, std sys	red	7	2	0	0	-0	-1
X=1.0, std sys	blue	-3	-1	-1	-0	1	-4
X=1.0, +1% sys shift	red	-24	-20	-8	-1	1	0
X=1.0, +1% sys shift	blue	7	16	19	20	18	12
X=1.8, std sys	red	-21	-10	-2	-0	0	1
X=1.8, std sys	blue	8	8	4	2	-1	6
X=1.8, +1% sys shift	red	-50	-30	-10	-2	1	2
X=1.8, +1% sys shift	blue	16	24	24	22	15	22

5. From Counts to Flux

The previous section laid out the origins of ADU count variability from one observation to another. Now we will consider how we can, in practice, acquire the information necessary to convert a particular observed ADU count to a measurement of $F_\nu(\lambda, t)$ above the atmosphere for a particular object. This requires measuring and then compensating for the variations in $S^{atm}(\lambda, alt, az, t)$ and $S_b^{sys}(\lambda, x, y, t)$. Let us first consider measurement of the variations in the hardware throughput curve, $S_b^{sys}(\lambda, x, y, t)$.





5.1. Measuring the Hardware Response

To measure the wavelength-dependent hardware response curve as a function of position in the focal plane, we will use a dome-screen system that is capable of producing narrow-band light over a range of wavelengths, producing a data cube of ‘narrow-band flat fields’. A similar approach has already been employed at PS-1 ((Stubbs & Tonry 2012); (Tonry et al. 2012)), and at DES ((Marshall et al. 2013)) After applying the monochromatic illumination correction (see Section 5.1.1) and applying the normalization at each wavelength from the photodiode monitors (see Section XX), this data cube records (up to an overall normalization constant) $S_b^{sys}(\lambda, t)$ at each x, y location in the focal plane. This data cube of narrow-band flats is used to construct a synthetic flat field by combining the individual narrow-band flats according to a chosen spectral energy distribution. Since the first stage of the calibration process, that which processes the actual pixels, assumes that sources have flat SEDs, we construct our synthetic flat with a flat SED propagated through a mean model atmosphere to the entrance pupil of the telescope. We call this flat the ‘flat spectrum flat’ (FSF).

Generation of the entire data cube of narrow-band flats is too time-consuming to complete on a daily basis. Instead, the full narrow-band flat field scan will only be repeated on a time interval adequate for measurement of the more slowly variable components of $S_b^{sys}(\lambda, t)$, approximately monthly (but to be determined during commissioning). Since the system response can change on shorter timescales, principally due to a changing population of dust particles on optical surfaces, we correct the FSF nightly by multiplying by the ratio of two broad-band flats, one at the current epoch and one at the reference epoch when the narrow-band flats were acquired.

5.1.1. Determining the Illumination Correction

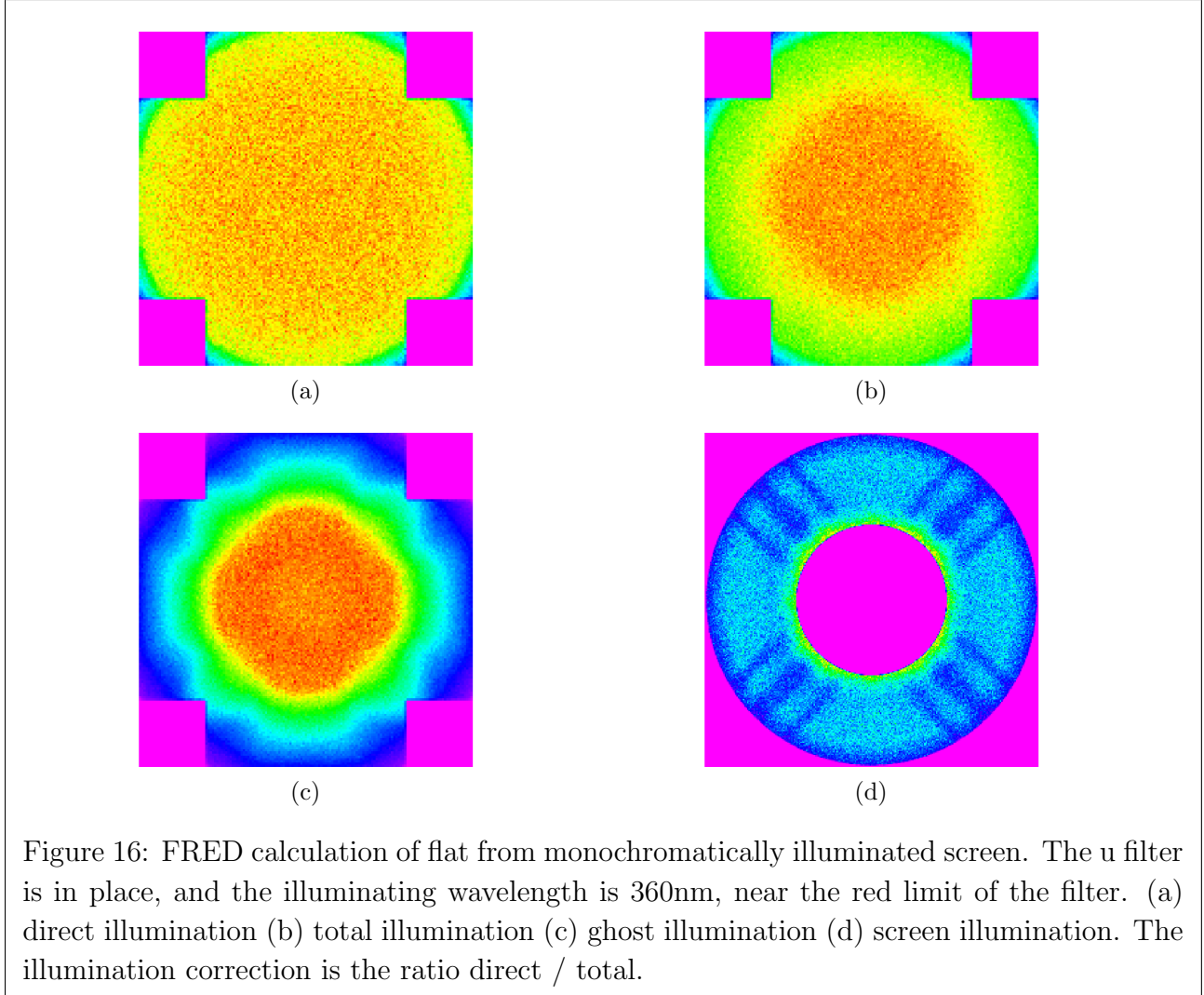
As mentioned above, before dome flats (either broadband or narrow-band) can be used to measure S_b^{sys} , they must be modified to correctly produce *photometrically* uniform measurements of a collimated source across the field of view. This correction is called the ‘illumination correction’. The illumination correction must correct the observed flat fields for effects resulting from non-uniform illumination of the dome screen, for ghosting caused by internal reflections in the camera, and for the presence of stray or scattered light arriving in the focal plane on paths other than the direct image path (such as light bouncing from the dome floor or glinting off a filter holder). Figure 16 gives a perspective on the difference between the direct, total, and ghost flatfield illumination from a realistic model of the LSST telescope, camera, and domescreen illumination system.

The illumination correction is difficult to measure directly. To do so would require a collimated light source with diameter small compared with the telescope pupil that is able to scan in pupil position, angle, and wavelength. Aside from the engineering challenges in producing such a light source in the dome, the resulting 5-dimensional data cube would require an inordinate amount of time to collect, and we have deemed this approach impractical. Instead, we plan to combine data from several paths to generate an illumination correction which is consistent with all of them:

- Detailed monte carlo optics models, such as FRED
- Laboratory measurements of the as-built camera with the CCOB (see Appendix X). This provides the detailed data cube envisioned above, but only for the camera in isolation. This is sufficient to characterize ghosts, but not scattered light in the full system.
- Raster scans of star fields in photometric conditions. The star fields will be chosen to be dense, without compromising photometry due to crowding, and to contain a wide range of colors.
- Second order corrections from running self calibration. Self calibration is particularly capable at determining corrections which are position dependent but wavelength independent, such as arise from nonuniform illumination of the dome screen (see Figure 18).

This process will consume significant amounts of time in the lab, time on the sky, and time in analysis. Fortunately, the illumination correction is expected to be stable with time and will be remeasured only when components in the optical path of the telescope are altered.

Because the illumination correction is wavelength dependent (highly so near the edges of the filter bandpasses), its effect on photometry is dependent on the SED of the object in question. Figure 17 shows this effect as a function of both radius in the focal plane and star color, for a set of Kurucz main sequence stars. The effects are clearly too large to ignore, or they would overwhelm the error budget. This is discussed further in Section 8. It seems likely that the quality of the illumination corrections is currently limiting the photometric accuracy of large surveys, and we expect the LSST treatment of the illumination correction to yield significant improvement.



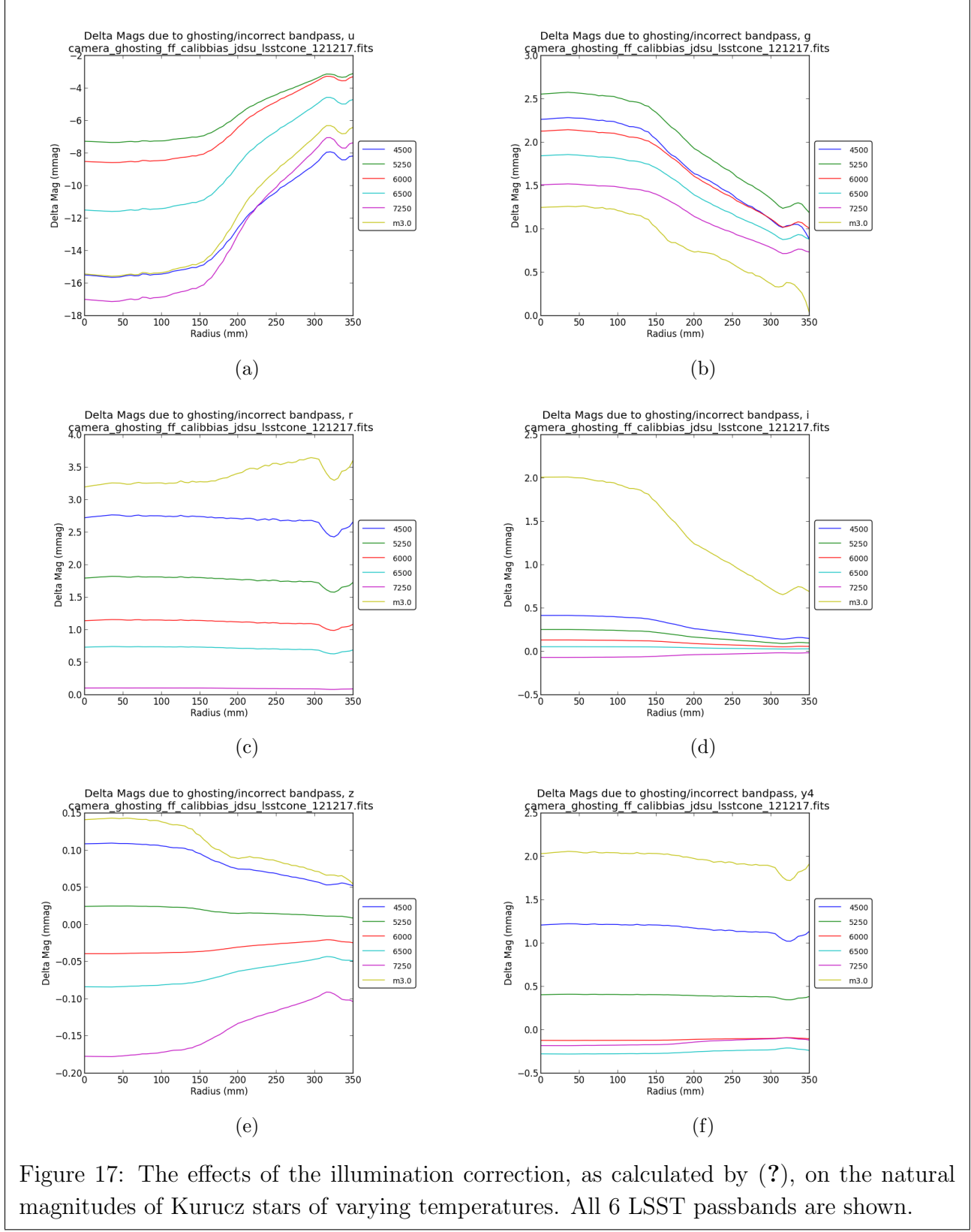


Figure 17: The effects of the illumination correction, as calculated by (?), on the natural magnitudes of Kurucz stars of varying temperatures. All 6 LSST passbands are shown.

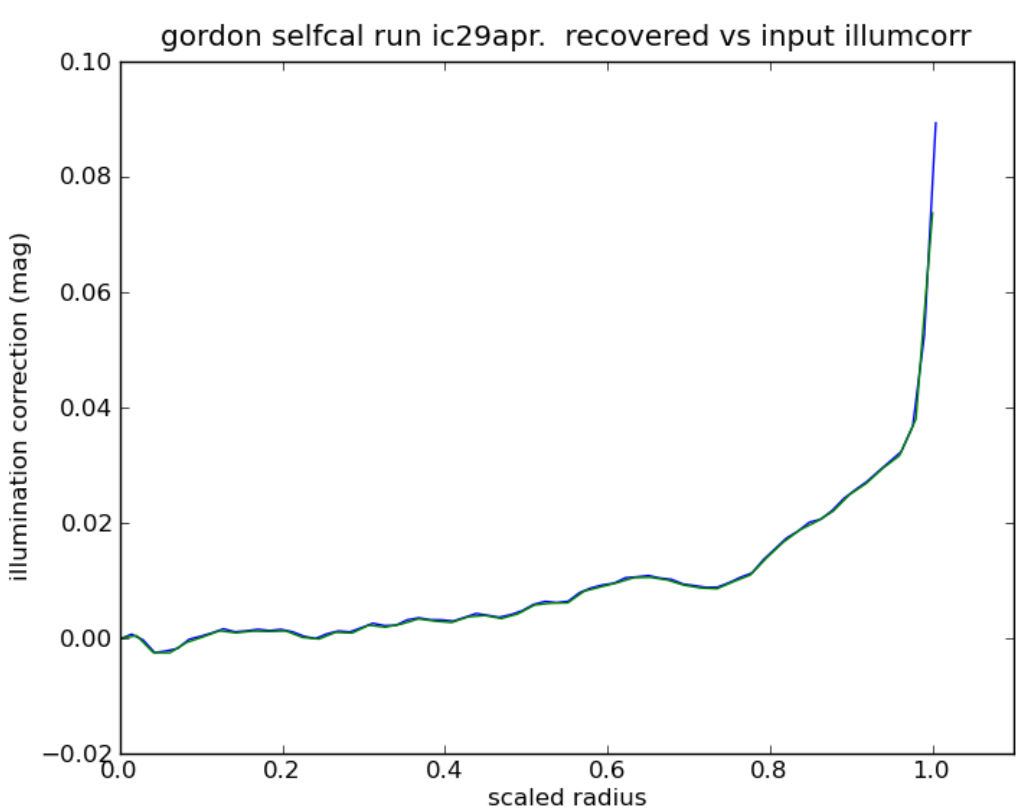


Figure 18: Recovery of input broadband illumination correction by self calibration. The input illumination correction was wavelength independent, but strongly dependent on radial position, as shown. The recovered illumination correction is essentially identical to that input.

5.2. Measuring the Atmospheric Transmission

Next, considering $S^{atm}(\lambda, alt, az, t)$, we will again separate the measurement of the shape of the atmospheric response and the measurement of normalization of the transmission. The currently available data is still incomplete, but suggests that the wavelength-dependent variations in $\phi^{atm}(\lambda, t)$ change smoothly over spatial scales larger than the field of view and over several minutes. By using an auxiliary telescope equipped with a spectrograph to observe bright stars with known SEDs, we can measure atmospheric absorption at a variety of positions in the sky every 5–10 minutes throughout the night. These observations are used as constraints for MODTRAN atmospheric models, generating representations of the atmospheric throughput in the form of a set of absorption components as a function of alt, az, t . These components can be interpolated in time and space to generate a wavelength-dependent atmospheric absorption profile, $\phi_b^{atm}(\lambda, alt, az, t)$, for each observation.

This approach has been put into practice by Burke et al ((Burke et al. 2010)). Probe stars were selected in the range $9 < V < 12$, and spectra were taken on a 1.5m telescope with a $R \approx 400$ resolution spectrograph. Exposure times were 2 to 4 minutes. The observing pattern is shown in Figure 19. The atmospheric model was a simple linear combination of templates generated by Modtran4 for molecular scattering, molecular absorption, aerosols, ozone, and water vapor. The models, together with some factors to account for the spectrograph efficiency as a function of wavelength, were fit to all the observed spectra simultaneously. Figures x and y show some results. The fit to the individual spectra are impressively good, and the coefficients in the resulting atmospheric models show strong variation, as expected for the highly variable nights for which the data was obtained. Traditional extinction plots (Figure z), show behavior that would be well fit by traditional calibration in the r- and i-bands, together with behavior in the z- and y-bands that would not. In subsequent development of the approach, Burke et al ((?)) obtained probe star spectra while simultaneously imaging over a wide field - roughly comparable to LSST operations. Unlike LSST, however, the imaging exposures were managed to keep the pixel coordinates of a given star nearly constant for all exposures. The full calibration process on the imaging data, including both atmospheric fitting and gray extinction determination through self calibration, yielded repeatability of approximately 8 mmag - good enough to meet the SRD minimum requirement for repeatability.

5.3. Self Calibration

In order to correct for the more rapid gray-scale variations in the relative normalization of $S^{atm}(alt, az, t)$ due principally to cloud extinction, we must use the observations of

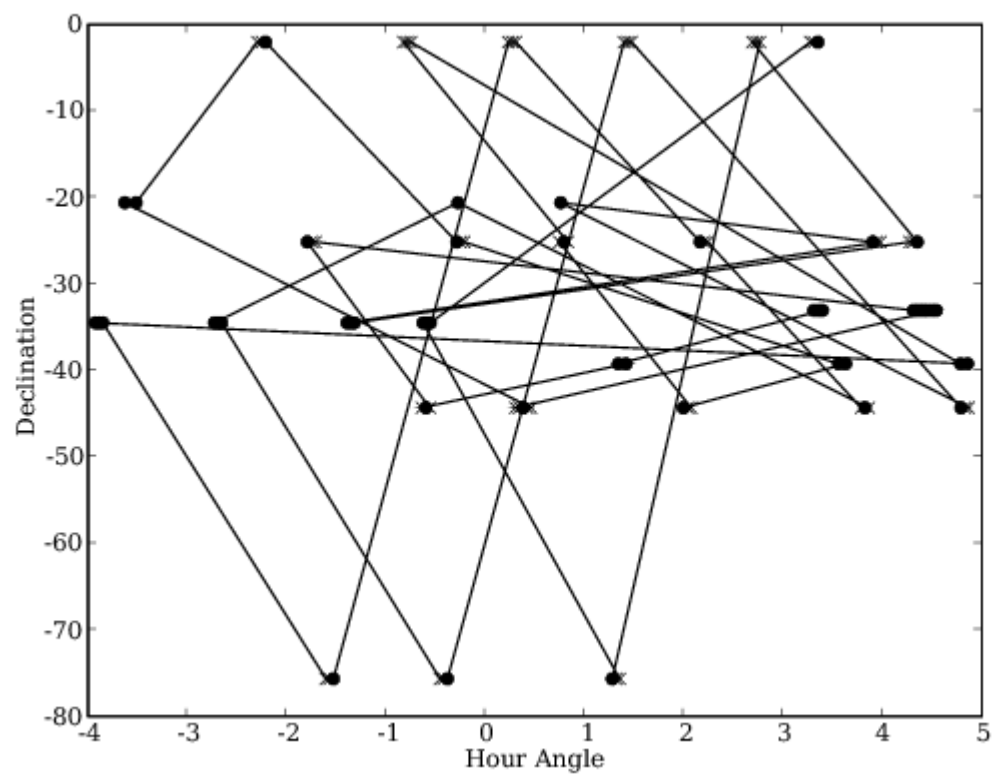
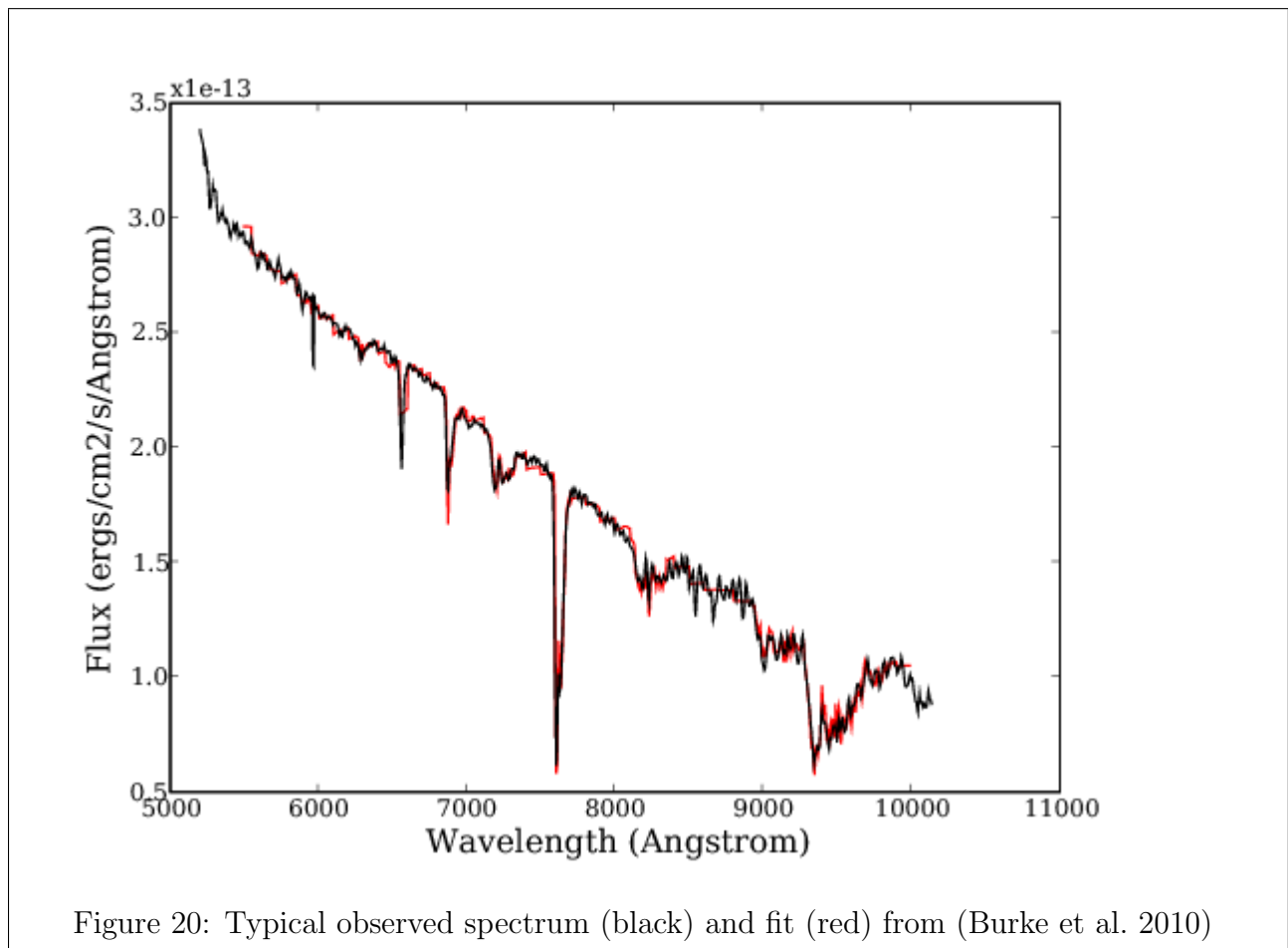


Figure 19: Pattern of observing atmospheric probe stars from (Burke et al. 2010). The Solid lines trace the temporal order of the observations



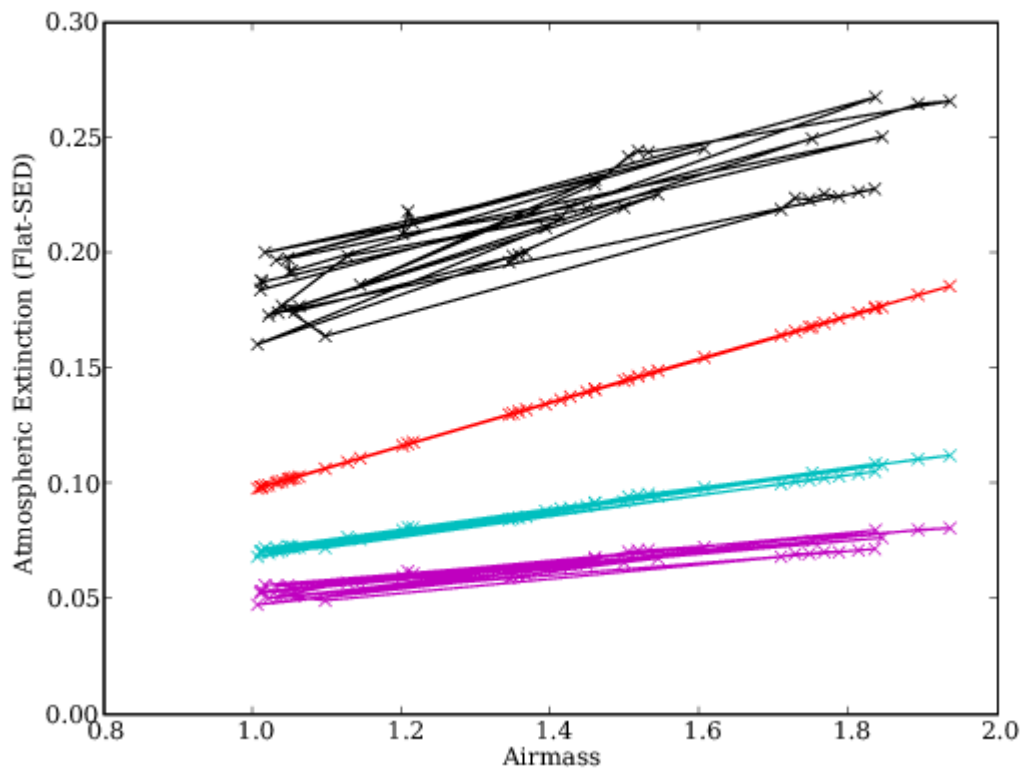


Figure 21: Non-gray atmospheric extinction from (Burke et al. 2010). Red is r-band, cyan is i-band, magenta is z-band, black is y-band.

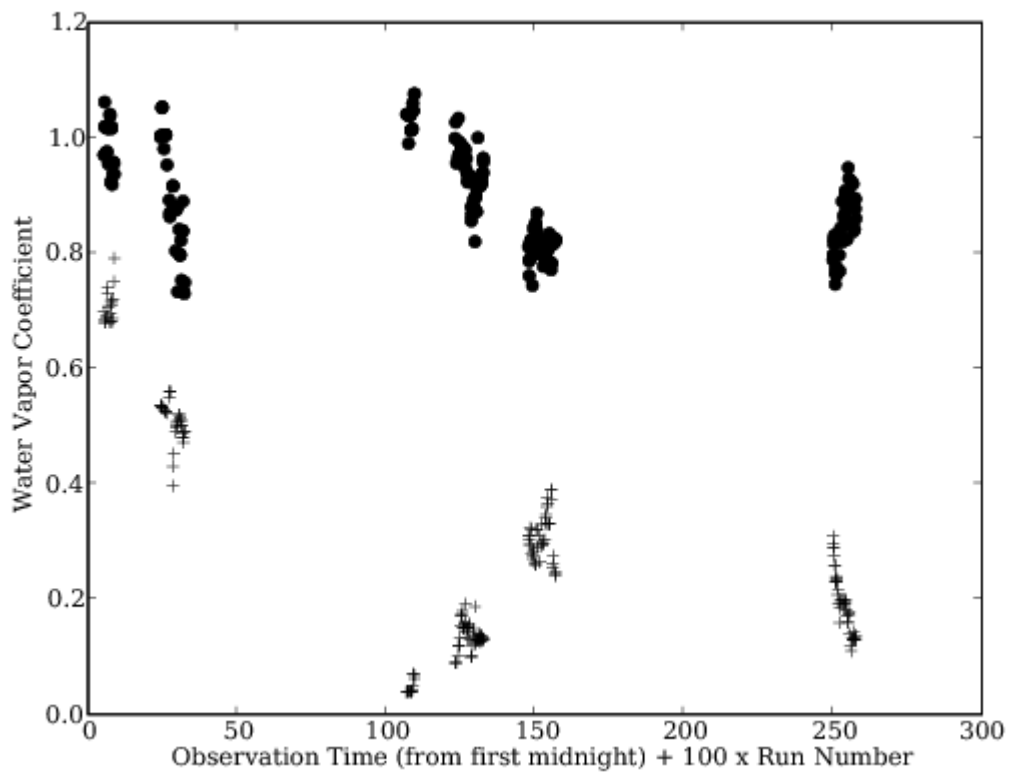


Figure 22: Fitted water vapor coefficient from (Burke et al. 2010), expressed as a ratio to the standard value (filled circles). Crosses are relative humidity from CTIO (changed scale).

calibration stars in the images themselves, as observations ((?), (Ivezić et al. 2007)) suggest that cloud extinction can vary by 0.01 magnitudes on the scale of a CCD on timescales as fast as a few minutes. This ‘self-calibration’ procedure could be thought of as creating a massive calibration ‘standard’ star catalog, where the calibration stars are a selected set of the non-variable, main-sequence stars in the science images; their main difference from true standards is that the true magnitudes of the calibration stars have to be bootstrapped from the many different observations of the survey, and their SEDs need to be inferred from multicolor photometry. For every calibration star, corrections for $\phi_b^{sys+atm}(\lambda, t)$ must be applied to produce a standardized magnitude, m_b^{std} , then in the self-calibration procedure we minimize the difference between the standardized magnitude and a model magnitude,

$$\chi^2 = \sum_{ij} \left(\frac{m_{b,ij}^{std} - m_{b,ij}^{model}}{\sigma_{b,ij}^{std}} \right)^2 \quad (18)$$

where the model magnitude is derived from the best-fit ‘true’ magnitude of the calibration star and a model describing how we expect the magnitude to vary from observation to observation. In the simplest self-calibration plan, this model simply consists of a normalization constant (zeropoint offset) for a ‘patch’ equivalent to the size of a CCD,

$$m_{b,ij}^{model} = m_{b,i}^{best} - \delta z_{b,j}. \quad (19)$$

This produces best-fit magnitudes for the calibration star catalog as well as zeropoint offsets (normalization constants) for each CCD in every observation, allowing us to correct for atmospheric extinction on the scale of a CCD. By adopting a more complex model, this procedure can also correct for variations in the relative normalization of the total system throughput beyond those contributed by cloud extinction (such as remaining errors in the illumination correction for the broadband and narrow-band flat fields), but is generally limited by the number of stars and number of observations of each star that are obtained. A CCD size patch provides several hundred stars calibration stars per patch, allowing good signal to noise when determining cloud extinction which varies from observation to observation. This is similar in nature to the ubercal method applied to SDSS in Padmanabhan et al. (2008), and more recently DLS (Wittman et al. 2012) and PanSTARRS-1 (Schlafly et al. 2012).

TODO: Need to discuss healpix implementation, etc

Repeating Equation 15 above, adjusting *obs* indexes to *meas* to reflect the difference between the true and measured quantities,

$$m_b^{std} = m_b^{inst} - \Delta m_b^{meas} + Z_b^{meas} \quad (20)$$

we can relate the terms in this equation to the corrections just described above. Δm_b^{meas} originates from the difference between $\phi_b^{meas}(\lambda, t, x, y)$ and $\phi_b^{std}(\lambda)$ convolved with the source

SED, and thus it depends on the shape of the total system response as well as the shape of the source SED. Δm_b^{meas} will be calculated by combining a series of model SEDs with $\phi_b^{meas}(\lambda, t, x, y)$ at various locations in the focal plane, creating a lookup table of values to apply to measured magnitudes. The Z_b^{meas} zeropoint offset comes from any normalization constants generated by the self-calibration procedure (in the simple model, just the $\delta z_{b,j}$ in equation 19 above).

These standard magnitudes are calibrated for variations in the observed bandpass shape (where applicable) and relative normalization, thus are directly comparable from one observation to the next. However, they are not yet tied to an external physical scale or from one filter band to another, and thus only define an internally calibrated LSST magnitude in a particular filter.

To fulfill SRD requirements 3 and 4, these internally calibrated natural magnitudes must also be tied from one filter band to another, and then tied to an absolute external physical scale. For this, a further set of measurements is needed. In all filters, a set of spectrophotometric standards must be observed, and calibrated using the steps described above. Then the known SED is combined with the standard bandpass shape to generate synthetic color photometry. The synthetic colors are then compared with the calibrated measured standard magnitudes to calculate Δ_{b-r} , the corrections needed to tie measurements in each filter together (referenced to r band). At this point, only one final measurement is necessary to tie the entire system to an external physical scale: an r band LSST natural magnitude measurement of an absolutely calibrated source on a photometric night. Although in theory these last two steps could be done with a single externally calibrated object, on a single photometric night, a larger set of external reference objects with well known AB magnitudes will be used to reduce systematic errors. This defines an AB magnitude,

$$m_b^{AB} = m_b^{std} + \Delta_{b-r} + \Delta_r \quad (21)$$

which can be compared to absolute physical flux scales.

This text needs to be edited into the above section This self-calibration procedure can be successful only if patches overlap on the sky, so that the same star is observed on multiple patches. This means complete sky coverage is necessary to link all stars together into a rigid system, but also indicates that some amount of dither is required. These investigations have shown that dither patterns where the overlap is one quarter of the field of view or more produce results meeting the SRD requirements.

Note that $m_{b,i}^{best}$ and δz_j are constrained only up to an arbitrary additive constant. For convenience, this constant can be set so that stars have roughly correct AB magnitudes, however the goal after self-calibration is primarily to have a rigid, self-consistent magnitude

system, equivalent to the natural magnitudes. Accurately calibrating the internal magnitudes to an external scale is discussed in the next section, Section 6.

5.3.1. Photometric vs. Non-photometric data

Correcting for the color terms resulting from the difference between $\phi_b^{meas}(\lambda, t)$ and $\phi_b^{std}(\lambda)$ requires some preliminary measurement of the color of each calibration star (to within 0.02 magnitudes). This means we must either have some prior knowledge of the colors of each star (from Gaia, for example) or we must have some other method for measuring colors in the *ugr* bands relevant to determining metallicity and the color corrections detailed in Section 4.1, presumably by measuring the magnitudes of these stars in photometric data. Without this requirement, we could just combine all photometric and non-photometric data in the self-calibration routine, leaving the self-calibration solver to determine the appropriate δz_j to compensate for any non-photometric images.

Assuming that we must first identify and use photometric data to determine the colors of each object, this could proceed as follows. Identify all observations which were obtained in relatively photometric conditions by searching for images where the average scatter in magnitude measured for each source was less than some threshold (say < 0.05 magnitudes). Using these images and standard stars in these images, measure a preliminary color for each object. With this preliminary color, make a correction for Δm_b^{meas} and run the self-calibration solver for this (photometric) subset of the data. Iterate the results of the self-calibration solver to improve the color determination for each star, until the color measurement converges to within 0.02 magnitudes.

At this point, we have colors accurate enough to apply a Δm_b^{meas} correction sufficient to run self-calibration on all images, including the non-photometric data. There will be some data which is not calibrateable, due to a large amount of cloud extinction; these images will be identifiable by the low **END**

5.4. Calibration Operations

The sequence for photometric calibration is then:

1. Acquire a broadband flat in each filter at the start and end of each observing night. Generate a full, wavelength-dependent illumination correction for the flats on a much longer time interval (timescale to be determined, but much longer than monthly).

Apply the appropriate illumination correction to the broadband flat. Apply flat field to images directly.

2. After remaining image processing (bias correction, fringe correction, etc) extract ADU counts of sources from images.
3. Acquire the data cube of narrow-band flat field images, approximately monthly. Apply wavelength-dependent illumination correction. Measure $\phi_b^{sys}(\lambda, t, x, y)$.
4. Acquire spectra of known stars roughly every 5–10 minutes throughout each night, fit for atmospheric absorption coefficients and generate $\phi_b^{atm}(\lambda, t)$ for each science images.
5. Combine ϕ_b^{atm} and ϕ_b^{sys} with a range of model SEDs to create lookup tables for Δm_b^{meas} for various locations in the focal plane.
6. At appropriate intervals (such as at Data Releases), run the self-calibration procedure, applying Δm_b^{meas} to stars chosen for self-calibration procedure and minimizing χ^2 from equation 18.
7. Apply appropriate Z_b^{meas} (and potentially Δm_b^{meas} values) to all objects in Data Release catalog, producing standardized magnitudes.
8. Apply measured corrections Δ_{b-r} and Δ_r , producing absolutely calibrated magnitudes.

This results in calibrated m_b^{AB} values in a standardized bandpass shape, with above-the-atmosphere fluxes.

6. Fixing LSST to an external scale

The next two subsections describe how the internally calibrated natural magnitudes, independently calibrated in each filter bandpass, are fixed to an external scale such that the flux in a single band can be compared to the flux in another filter band (SRD requirement 3) and that the flux in a particular filter band can be compared to an absolute external system (SRD requirement 4). This is equivalent to determining Δ_{b-r} and Δ_r from Eqn 21.

Standard stars enter this process in these ways...

6.1. Band to band (color)

The band to band calibration for each filter b (the Δ_{b-r} values) will be determined by measuring the flux from one or more celestial objects whose physics are believed to be well understood. In principle, a single object with known colors would be sufficient, however many objects across the LSST footprint will be used to evaluate possible systematic effects in the internal calibration process.

Hot hydrogen (DA) and helium (DB) white dwarf stars have simple atmospheres that are reasonably well understood (model colors are currently reliable to about 0.01 magnitudes). It is estimated that there will be $\approx 100/10$ DA/DB WD stars with $r < 24$ in each LSST image at the South Galactic Pole. Although in theory only one WD with high resolution spectroscopy would be required to calibrate colors for the entire survey, on the order of 100–1000 across the sky will be used to search for systematic effects. Catalogs of WD stars visible from Cerro Pachon have been constructed (Bergeron 1992; Bohlin & Gilliland 2004), and a ‘white dwarf calibration system’ has been developed (Holberg & Bergeron 2006). The locus of main sequence stars in color-color space is also reasonably well understood and has been used to calibrate photometry with success in previous surveys (MacDonald et al. 2004; Ivezić et al. 2007). The use of the main sequence stellar locus in addition to WD stars will provide a valuable check on systematic effects that may arise from using (primarily) white dwarfs in the determination of $\phi^{atm}(\lambda, alt, az, t)$, as white dwarfs are bluer than most of the main sequence stars used for the bulk of the remainder of the calibration procedures. Additional checks on the quality of color calibration will be based on color residuals when determining photometric redshifts for galaxies. Analyzing these residuals as a function of galaxy brightness and color, and across the LSST footprint, will yield detailed quantitative estimates of the calibration quality. Although in theory one well-measured standard is all that would be necessary to determine Δ_{b-r} values for each bandpass, in practice having multiple standard with varying colors will serve as a check on systematics and provide estimates of the calibration uniformity throughout the survey.

The values for Δ_{b-r} will be determined by generating model m_b^{std} values for each band-band calibration object, then minimizing

$$\chi^2 = \sum_i \left(\frac{(m_{b,i}^{std} - m_{r,i}^{std})^{meas} - (m_{b,i}^{std} - m_{r,i}^{std})^{model}}{\sigma_{b-r,i}} \right)^2. \quad (22)$$

This comparison can be done using subsets of objects from low Galactic extinction regions, and then bootstrapping to the entire sky to check for systematic effects.

6.2. Single bandpass to external flux system (absolute scale)

After determining the band to band calibration, there is one further value required to calibrate the entire system to an absolute flux scale: Δ_r . This could again be determined using a single object with a well-known flux and spectral energy distribution, however multiple external calibrators provide a valuable check on systematic effects.

Several WDs in the Northern hemisphere have been very precisely calibrated with HST STIS measurements (Bohlin & Gilliland 2004) and it should be possible to obtain similar HST measurements of one or more targets for use in the Southern hemisphere. Identification of these targets has not yet been completed. Nevertheless, as a result of calibration efforts to support the SDSS-II SNe survey, the absolute calibration of the SDSS Stripe 82 region in the r band is believed to be accurate at the 0.01 mag level (Frieman et al. 2008). **TODO Tim will update with Abi white dwarf standards details**

Another route to calibrating to an external flux system is to use standards from Gaia. These will have the advantage of being numerous and widely spread across the sky, with a useful overlapping magnitude range between $r = 16$ to $r = 20$. The magnitude measurements of stars calibrated with the LSST calibration procedure described in this document can be transformed to synthetic magnitudes in Gaia’s bandpasses and compared to Gaia measurements. **TODO Tim will update with more information on Gaia.** This comparison across the LSST footprint and as a function of stellar brightness and color will provide a powerful independent test of the quality of LSST photometric calibration.

7. Calibration Hardware

7.1. Flat Field Illumination System

The dome screen projector is an array of projectors mounted in the dome of the LSST enclosure, specially designed to provide very uniform illumination to the LSST étendue (the incoming aperture of the telescope, taking into consideration the desired angle of the incoming light) while minimizing any light straying beyond the étendue. In addition, the dome screen will be able to project both broadband and tunable narrow-band (essentially monochromatic) light sources, providing both broadband (broadband) and narrow-band flat fielding capabilities.

7.2. Auxiliary Telescope

reference figure of observing pattern from Burke 2010

Using MODTRAN we can generate atmospheric transmission profiles at a variety of airmasses for each of these major sources of atmospheric extinction – molecular (Rayleigh) scattering, aerosol (Mie) scattering, and molecular absorption from each of O₃, H₂O, and combined O₂/trace species, as is shown in Figure 27 for a standard atmospheric composition (the 1976 US Standard). These profiles capture the wavelength dependence of each component individually, over a grid of airmasses, and can be used as templates to generate new atmospheric transmission curves for any desired atmospheric composition as follows:

$$\begin{aligned} S^{fit}(alt, az, t, \lambda) = & e^{-\tau_{aerosol}(alt, az, t, \lambda) X} \\ & \times (1 - C_{mol}(BP(t)/BP_o) A_{Rayleigh}(X, \lambda)) \\ & \times (1 - \sqrt{C_{mol}(BP(t)/BP_o)} A_{O_2}(X, \lambda)) \\ & \times (1 - C_{O_3}(t) A_{O_3}(X, \lambda)) \\ & \times (1 - C_{H_2O}(alt, az, t) A_{H_2O}(X, \lambda)). \end{aligned} \quad (23)$$

The $A_{Rayleigh/O_2/O_3/H_2O}$ functions are absorption templates (i.e. 1 minus the transmission profiles from the MODTRAN models), the C_{mol,O_3,H_2O} are coefficients describing the composition of the atmosphere together with $\tau_{aerosol}$, and $BP(t)$ is measured. An example of an atmosphere generated in this fashion is shown in Figure 28, demonstrating that this method can be used to generate an atmosphere at any airmass for any composition desired, without needing to generate a full MODTRAN model.

With this capability, we can fit the auxiliary telescope spectroscopic data taken throughout the night for the values of C_{mol,O_3,H_2O} , increasing our SNR for these coefficients by modeling their expected behavior over time and across the sky as detailed in ?? above. The Rayleigh scattering and molecular absorption due to O₂ and other trace species are fit with a single coefficient, C_{mol} , which simply scales the MODTRAN templates to the appropriate level for Cerro Pachon, and then only change with the barometric pressure (BP). The O₃ absorption is fit with a single C_{O_3} value for each night, as it is not expected to vary more than 5-10% within a night. The aerosol absorption, as it is expected to have a small spatial variation across the sky, is modeled as

$$\tau_{aerosol}(alt, az, t, \lambda) = (\tau_0 + \tau_1 \text{EW} + \tau_2 \text{NS}) \left(\frac{\lambda}{\lambda_0} \right)^\alpha, \quad (24)$$

where EW and NS are defined as EW = cos(alt)sin(az), NS = cos(alt)cos(az), projections of the telescope pointing in the EW/NS directions. Single values of τ_0 , τ_1 , τ_2 and α are fit

for each night of observing, with τ_1 and τ_2 likely to be very small (Burke et al. 2010). The H₂O absorption is likewise expected to show spatial variation, but also time variability, and is modeled as

$$C_{H_2O}(alt, az, t) = C_{H_2O}(t) + \frac{dC_{H_2O}}{dEW} \text{EW} + \frac{dC_{H_2O}}{dNS} \text{NS} \quad (25)$$

using a constant spatial EW and NS gradient per night and a $C_{H_2O}(t)$ that is fit to each auxiliary telescope measurement (and interpolated between these times).

The coefficients $C_{mol/O_3/H_2O}$ and $\tau^{aerosol}$ will be determined using spectra of bright stars obtained from the 1.2-m LSST auxiliary telescope. The auxiliary telescope will be equipped with a modest resolution ($R \sim 400$) spectrograph, sufficient to capture the signatures of the atmospheric extinction components, and covering the entire wavelength range of LSST ($300 < \lambda < 1100$ nm) in each exposure. The stars observed with the auxiliary telescope must be bright ($r < 12$) and ideally either white dwarfs or F stars – stars with relatively simple and well-understood SEDs to minimize confusion with the atmospheric extinction. By observing the same grid of stars on multiple nights, even if the SEDs are not well determined initially, they can be bootstrapped from the many epochs of data.

Generally, the auxiliary telescope will *not* observe stars along the same line of sight as LSST, as the values for $C_{mol/O_3/H_2O}$ and $\tau^{aerosol}$ are better constrained by observing a wide variety of airmasses and locations on the sky that cover a wide range in N/S/E/W directions, as well as utilizing repeat observations of the same star throughout each night, and then fitting the spectroscopic data from the entire night. This improves the signal to noise for the atmospheric absorption profiles generated for each science observation.

The expected effect of $\phi_b^{atm}(\lambda)$ variations

Burke et al. (2010) describes a series of observing runs at CTIO carried out over several months, where spectroscopic observations of stars were fit using this method. Using the extremes of the range of C_{mol} , C_{O_3} , C_{H_2O} , τ_i and α parameters from these runs, Figure 29 shows the resulting changes in observed magnitudes due to the changes in bandpass shape when applied to our set of main sequence star Kurucz models. Varying C_{H_2O} only affects the z and y bands, while changing C_{O_3} , τ_0 , and α affect the u and g and, to a lesser extent, r bands. Using these ‘worst-case’ parameters, at $X = 1.2$ we find differences in the observed natural magnitudes on the order of $\Delta u = 14$ mmag, $\Delta g = 7$ mmag, $\Delta r = 4.5$ mmag, $\Delta i = 1.5$ mmag, $\Delta z = 2$ mmag, and $\Delta y = 7$ mmag. The atmosphere transmission curves used to generate this data, and a plot of the resulting Δm_b^{obs} are in Figures 30 and 31. These represent the induced changes in observed counts due to changes in the bandpass shape; however, by achieving 10% accuracy on $\tau^{aerosol}$, C_{O_3} , and C_{mol} , and 30% accuracy for C_{H_2O} ,

we can correct for these effects to within 1 mmag in all bands except y , where it remains 2 mmag. The limits on remaining uncorrected effects are shown in Figure 32.

7.3. Water Vapor Monitoring System

7.4. Camera System Telemetry

8. Calibration Error Budget

Many sources of errors feed into the calibration process. It is a challenging task to identify and quantify all of them, and we have not yet completely done so. We present our current estimates here, but they are subject to change as our analysis improves. We first discuss repeatability errors, and then uniformity errors. The band-to-band, and absolute calibration errors flow directly from the characteristics of the standard stars, and have already been discussed in Section 6.

8.1. Repeatability Errors

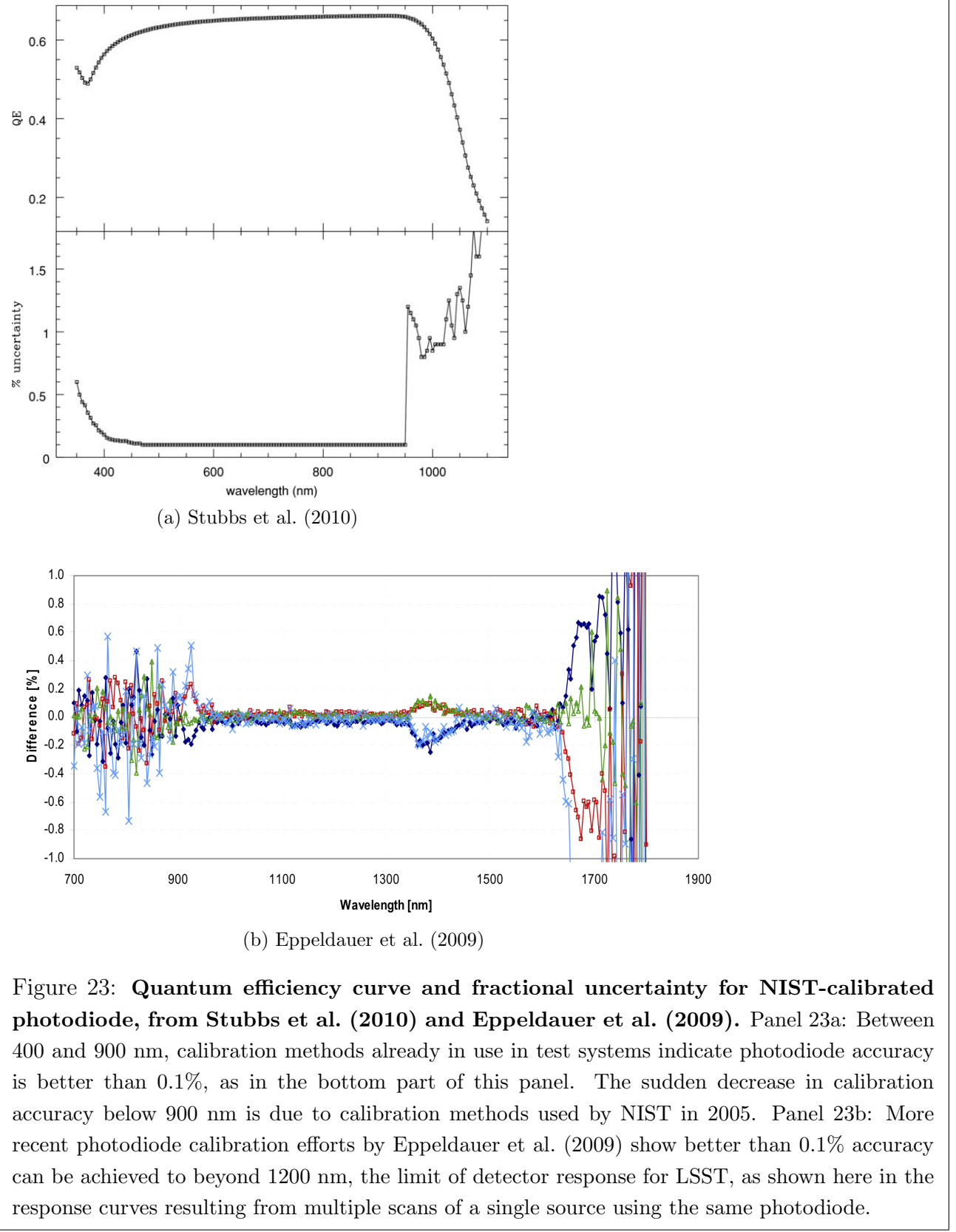
The repeatability error in m_b^{std} for individual calibration stars must meet the requirement in the SRD (Requirement 1 in Section 2). The contributions to this error are best discussed in the context of Figure 1. If we recall that

$$m_b^{std} = m_b^{inst} - \Delta m_b^{obs} + Z_b^{obs} \quad (26)$$

it is natural to divide the error sources into three categories:

- errors in m_b^{inst} , determined by Flat SED Calibration
- errors in Δm_b^{obs} , determined by SED Correction
- errors in Z_b^{obs} , determined by Self Calibration

We will assume that the errors in these terms are uncorrelated, and add in quadrature to produce the overall error.



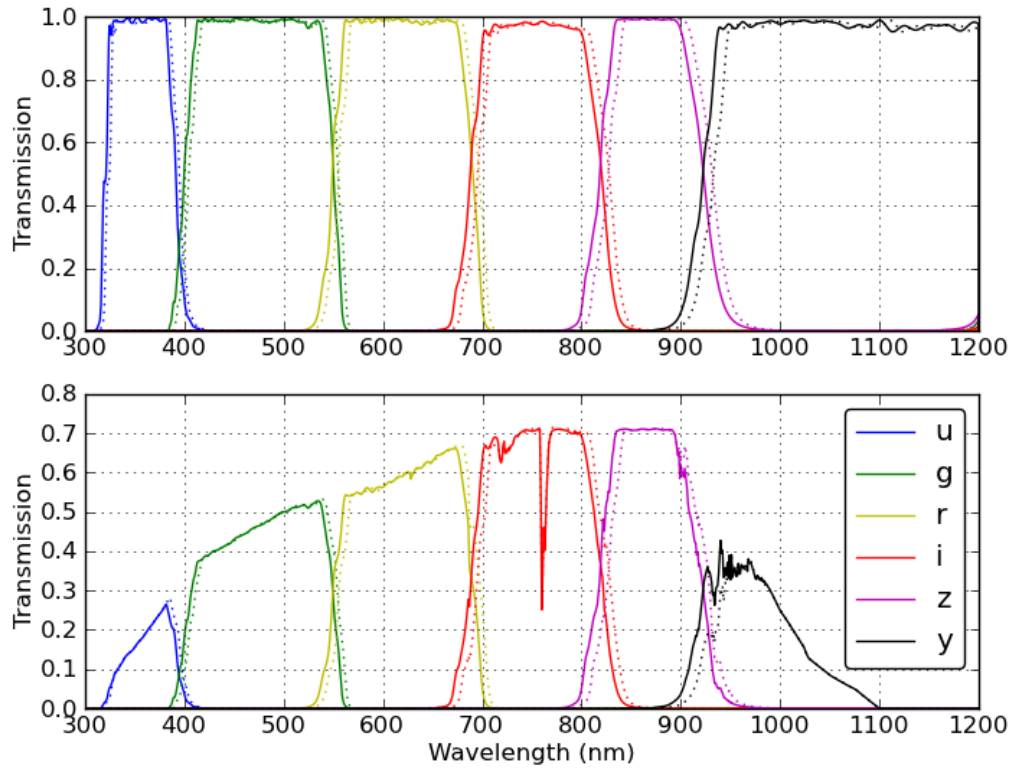
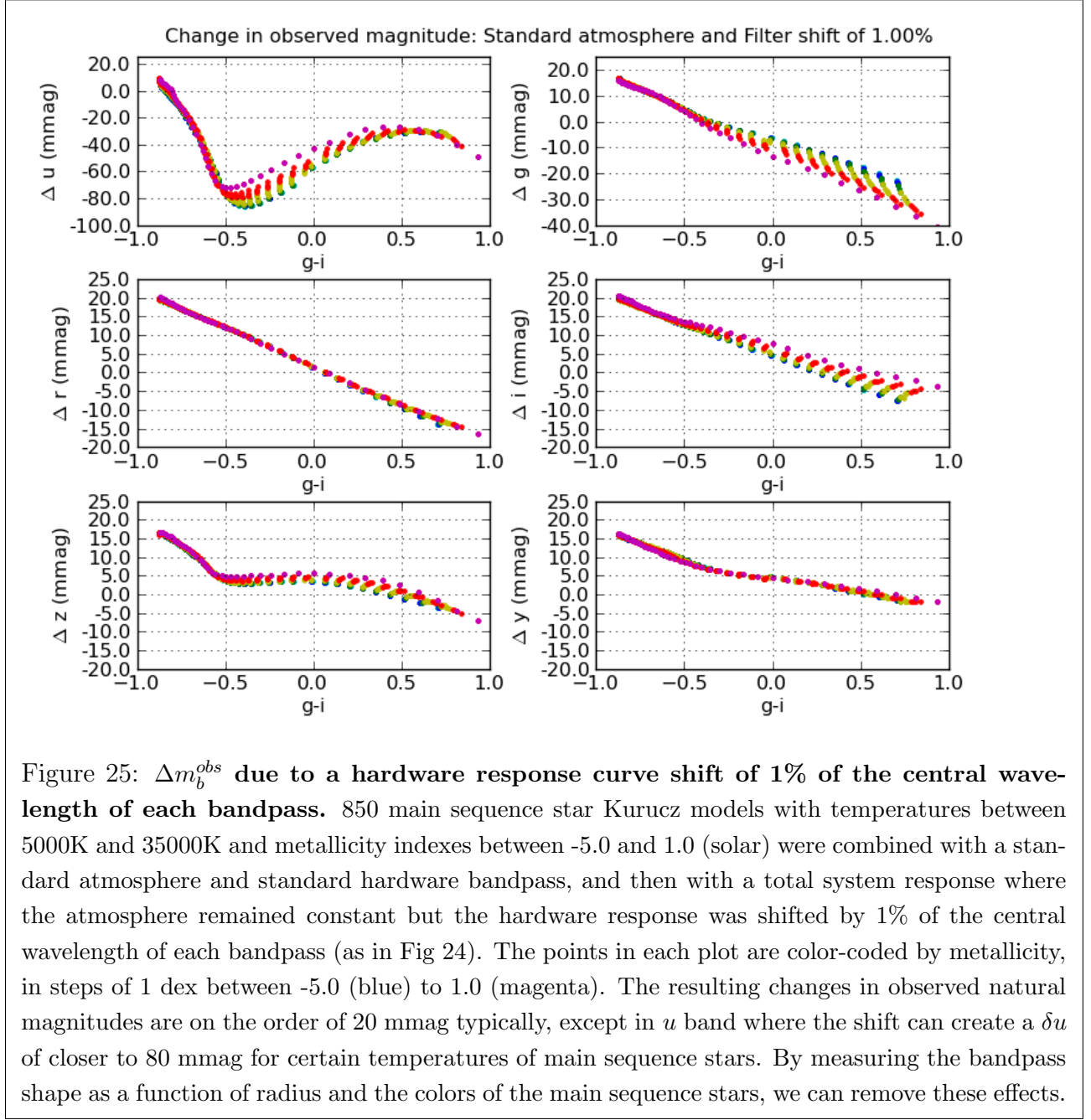
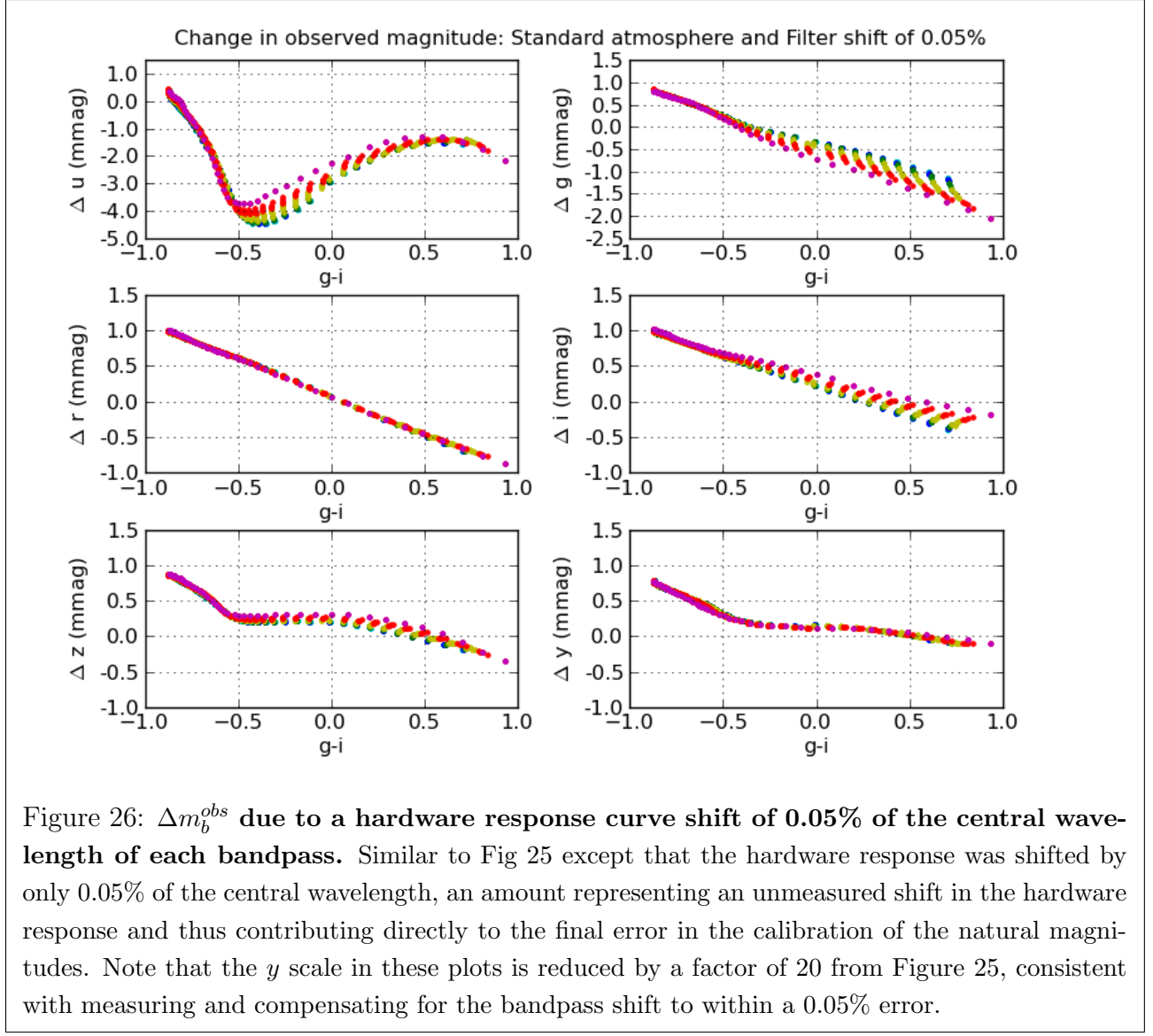
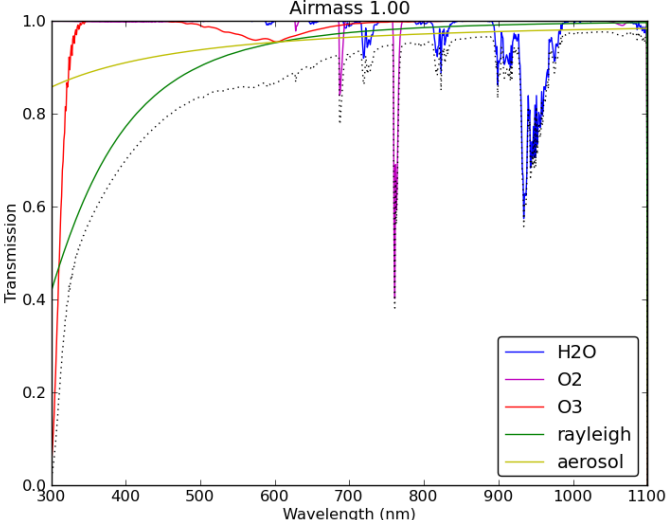


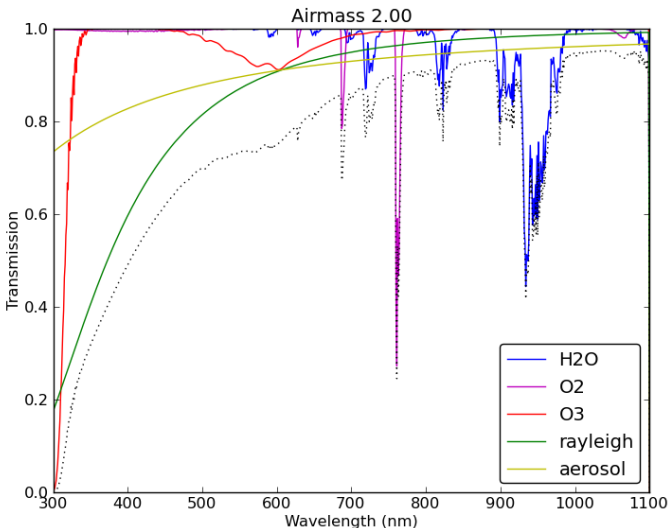
Figure 24: **Baseline filter curves and a potential (1% of the central wavelength) shift due to nonuniformity in the filter bandpass.** The solid lines indicate standard filter bandpasses (top panel: filter alone, bottom panel: filter plus standard mirror, lens, detector and atmosphere response curves) while the dashed lines indicate the same bandpass shifted redward by 1% of the central wavelength.







(a)



(b)

Figure 27: Components of atmospheric absorption. The wavelength dependence of various atmospheric absorption components at zenith (Panel 27a) and at airmass=2.0 (Panel 27b) are shown here. The H₂O (blue) and O₃ (red) molecular absorption contributions are shown separately, while the O₂ absorption is combined with other trace elements (magenta). A typical example of aerosol scattering (Mie scattering) is included (yellow), as is molecular scattering (Rayleigh scattering) (green). All components except aerosol scattering were generated using MODTRAN4 with the US Standard option (aerosol scattering is not part of the US Standard atmosphere). The resulting total absorption curve is the product of each of these effects and is shown with the dotted black line. This is an illustrative atmosphere; under actual observing conditions the molecular absorption components will vary in strength with time and the square root of the airmass, the molecular and aerosol scattering will depend on airmass, and the aerosol scattering profile will also vary with time.

8.1.1. Errors in m_b^{inst}

As sketched in Figure 1, m_b^{inst} is produced by the LSST Data Management System (DM), through processing raw science exposures. Leading error contributions come from the flat spectrum flat (modulated by position and PSF changes of the star on the focal plane), sky background subtraction, and the photometry algorithm used to extract source counts from the flattened and sky-subtracted image. We do not attempt to quantify those individual contributions here, in good part because the relevant software is still early in its development process within DM. Rather, we note that photometric errors, considered as a function of stellar magnitude, always display a systematics floor at the bright end. The contribution of this error to repeatability can not be reduced by any part of the subsequent calibration process, and adds in quadrature to the repeatability error estimate. The estimate from DM is that this error floor will be 3mmag.

8.1.2. Errors in Δm_b^{obs}

As shown in Section 5, Δm_b^{obs} is a function both of the system bandpass, ϕ_b^{obs} , and the SED of the object, $F_\nu(\lambda, t)$. It is affected by the following errors:

- Errors in the atmospheric bandpass, S^{atm}

- Errors induced by measurement noise in atmospheric probe instruments (auxiliary telescope; water vapor monitoring system)

Measurement errors from the water vapor monitoring system are expected to be +/-1mm. Making use of the plots in Figure ??, which is for a variation of 5mm, this translates to errors of 0.2 mmag in u-band, negligible in g,r, and i-bands, 1 mmag in z, and 2mmag in y.

We do not yet have reliable error levels for aerosols and ozone. Based on the data from (Burke et al. 2010), we estimate that the errors are no more than 10% of the total variation seen in each of those components, RSSed together. Figures ?? and ?? show that the resulting errors are roughly 1.6 mmag in u-, 2.1 in g-band, 0.1 in r, and negligible in all other bands.

- Unmodelled spatial and/or temporal variation of atmospheric components, particularly aerosols

The water vapor extinction is measured along the LSST’s line of sight by the co-pointed microwave radiometer, so it is not subject to this error. For aerosols

we again take 10% of the total variation seen. this gives 1.4 mmag in u, 0.7 mmag in g, and negligible for others.

- Errors in determination of monochromatic illumination correction, which propagate directly into errors in S_b^{sys} .

If the monochromatic illumination correction was ignored, the resulting errors in Δm_b^{obs} are as shown in Figure ???. The maximum effect is roughly 15mmag in u-band and 3mmag or less in the other bands. As discussed in Section 5.1.1, we will determine the illumination correction from a combination of modelling and dedicated measurements. While the accuracy of the result is difficult to assess in advance, we conservatively assume that the error will be 20%. This results in an error contribution of 3mmag in u-band, and 0.6mmag in the others.

- Wavelength-dependent errors in measurement of the domescreen intensity by the photodiode monitor. This will result in errors in combining the monochromatic domeflats to determine S_b^{sys} .

A photodiode monitor for this purpose was first employed by Stubbs on the PS-1 telescope ((Stubbs et al. 2010)), and an error analysis was undertaken. We are sensitive to systematic errors in the photodiode response rather than to noise, which can be effectively averaged over. Figure ?? estimates the level of these systematic errors as 2 mmag at 400nm, 1 mmag between 470 and 950nm, and increasing beyond 950nm to 10 mmag. Figure 36 shows the effects on Kurucz SEDs of a randomly chosen systematic error curve that conforms to these levels. The effects are negligible in all but the u-band.

- Errors in determining the SEDs of calibration stars from their multicolor photometry.

In practice, Δm_b^{obs} for a calibration star will be determined by looking up its SED as a function of a set of colors formed from the 6 band magnitudes, and then integrating against the system bandpasses ϕ_b^{obs} and ϕ_b^{std} according to equation ???. The SEDs will come from some model of main sequence (MS) stars (we have been using Kurucz in our work). Real stars deviate from the canonical main sequence (MS) locus, however, due to many causes. Intrinsic widths of the MS color-color locus are generally estimated to be on the order of 20mmag ((??)). This translates directly into an error in Δm_b^{obs} . For example, if we use Figure ?? as an indication of the maximal expected values of Δm_b^{obs} , we can multiply the maximum slope in each band by 20mmag to get an estimate of the effect. The values of the maximum slopes are roughly: 0.28 (u), 0.04 (g), 0.02 (r), 0.02 (i), 0.02 (z), 0.01 (y). This leads to the values in Table 2. This error source is negligible for all but the u-band, where it contributes significantly to the error budget. It is likely that a more careful choice of SED models can reduce this error term.

- Effects of contamination buildup between monochromatic domeflats

Still TBR. This will likely determine the required frequency of taking monochromatic domeflats

- Effects of uncertainties in focal plane temperature on wavelength-dependent detector QE

The detector QE at wavelengths near the red cutoff is affected by temperature, with higher temperatures resulting in higher QE. The focal plane temperature is monitored by the camera, allowing the temperature at any point on the focal plane to be predicted to 0.5 deg K with respect to the reference condition when the monochromatic dome flats were obtained. Figure 35 shows, as expected that the effect of that prediction error on the natural magnitudes is negligible for all but the y-band, where it is 0.2 mmag. There is, of course, a larger effect on the zeropoints, discussed below.

8.1.3. Errors in Z_b^{obs}

Every exposure has a spatial zeropoint model determined by Self Calibration as the solution to a large linear least squares problem, as discussed in Section 5. The errors in the zero points are dependent on the spatial scale of the perturbations, as one can see from a simple argument. One can reasonably expect that Self Calibration will determine the true magnitudes of the calibration stars with an error that is well below the repeatability requirement ($\sigma \approx 5$ mmag) for individual measurements, so for present purposes we ignore the errors in the true magnitudes. Suppose a perturbation shifts, for a single exposure, the zeropoint over an area A by some constant δZ . If that area contains N calibration stars, each provides an estimate of δZ with an error of σ . The full set of calibration stars, assuming that their measurement errors are uncorrelated, allows δZ to be estimated to a precision of $\sigma_{\delta Z} = \sigma/\sqrt{N}$. The density of calibration stars varies over the sky. Here we will use a mean value of 2 arcmin^{-2} , which corresponds to stars in the range $20 > V > 18$ at galactic latitude of 30 degrees. This provides the following rough estimates for spatial scales of relevance:

- Detector segment: $A = 11 \text{ arcmin}^2$, $N \approx 22$, $\sigma_{\delta Z} \approx 1$ mmag
- Detector: $A = 178 \text{ arcmin}^2$, $N \approx 356$, $\sigma_{\delta Z} \approx 0.25$ mmag
- Focalplane: $A = 3.4 * 10^4 \text{ arcmin}^2$, $N \approx 6.8 * 10^4$, $\sigma_{\delta Z} \approx 0.02$ mmag

This makes it clear that the size of a detector segment is a rough boundary, above which zeropoint errors should be negligible, while below it they may become quite significant. In

reality, many zeropoint perturbations (such as clouds and focal plane temperature variations) have a continuous spatial power spectrum, and a more sophisticated estimate is required.

We have determined the attenuation factor from simulations of the Self Calibration process (Section 9). Additionally, Gauss-Markov analysis (show results?) **EXPAND**

Note that, to first order, zeropoint errors are expected to depend on their spatial scale, but *not* on magnitude of the zeropoint perturbations that drive them. This expectation is confirmed by Figure ??.

Perturbations to the zeropoints arise from:

- Clouds, and the varying gray averages of extinction from aerosols, water vapor, and ozone
- Camera gain variation
- Shutter travel time variation
- Detector QE variation due to varying focal plane temperature

8.2. Uniformity Errors

The uniformity errors must meet the uniformity requirement in the SRD (Requirement 2 in Section 2). These are driven by systematic errors in Z_b^{obs} and Δm_b^{obs} . There are several sources:

- errors in standards
- systematic variation of calibration star properties across the sky
- unmodeled systematic variations in the atmosphere

9. Testing and Verification

The calibration process presented above is complex, and meeting the SRD requirements is dependent on understanding and controlling a large number of small perturbations. We

Table 2:: Repeatability error budget. All values are in mmag

Affected term	Effect	<i>u</i>	<i>g</i>	<i>r</i>	<i>i</i>	<i>z</i>	<i>y</i>
m_b^{obs}	Total	3.0	3.0	3.0	3.0	3.0	3.0
Δm_b^{obs}	Atmospheric water vapor errors	0.2	0	0	0	1.0	2.0
	Atmospheric aerosol and ozone errors	1.6	2.1	0.1	0	0	0
	Undetected atmospheric variability	1.4	0.7	0	0	0	0
	Monochromatic illumination correction errors	3.0	0.5	0.8	0.5	0.1	0.6
	Photodiode monitoring system errors	0.8	0.5	0	0	0	0.1
	Calibration star SED errors	5.6	0.8	0.5	0.4	0.4	0.2
	Focal plane temperature errors	0	0	0	0	0	0.2
	Total	6.7	2.5	0.9	0.6	1.1	2.1
Z_b^{obs}	Clouds						
	Camera gain variation						
	Shutter variation						
	Temperature induced QE variations						
	Errors in standards						
	Total						
Total		7.4	3.9	3.1	3.1	3.2	3.7
Design Requirement		7.5	5.0	5.0	5.0	7.5	7.5
Min. Requirement		12	8.0	8.0	8.0	12	12

seek to verify that our approach will produce the required results, and are doing so with different techniques that apply to the stages of LSST’s construction and operation. During the current final design phase, we are employing simulation tools, backed up when possible by measurements on the sky from existing telescopes. (?) and (Burke et al. 2010) are examples of this approach. During the construction phase, we will be able to feed measured data from actual telescope components into the simulations. During operations, our focus is on designing metrics that will let us assess the calibration quality on an ongoing basis.

9.1. Self Calibration Simulation

9.2. Auxiliary Telescope Simulation

9.3. Calibration Performance Metrics

9.3.1. Repeatability

XXX-Testing our repeatability is rather trivial, as that does not require any external data. We simply apply the best-fit patch zeropoints to each patch and measure how well we make repeat measurements of each star.

9.3.2. Spatial Uniformity

XXX-We can compare to previous surveys. Pan-Starrs notes that they tend to see SDSS-shaped footprints in their residuals when comparing surveys. This will probably only put an upper limit on the uniformity, as LSST will be deeper and/or have larger coverage than available comparison surveys. Simulations can also help identify regions which we would expect could be poorly linked to the rest of the survey (this is expected to be a problem early in the survey before all regions of the sky have many well-linked observations). We can measure very accurately our RMS as a function of patch and magnitude, and thus generate mock catalog realizations to run through the self-calibration procedure. These mock catalogs should give a good picture of the spatial uniformity.

9.3.3. Flux Calibration

As mentioned in §6.2, there should soon be a system of white dwarf flux standards with HST observations. We can use subsets of these flux standards to make bootstrap estimates of our overall flux calibration. This is also a potential test of the spatial uniformity of the calibration, although this will be limited if the flux standards are concentrated on the equator.

9.3.4. Color Calibration

There are now a number of techniques for comparing stellar colors across the sky. Ivezić et al. (2004) use a principle color analysis, High et al. (2009) use a stellar locus regression,

and Schlafly et al. (2010) look at the color of main-sequence turn-off stars. For all of these techniques, the signal is usually dominated by dust extinction. However, at high galactic latitudes, the differences in stellar colors reveals errors in the calibration.

In addition to main-sequence stars, our flux standards should be useful for checking the color calibration. As with the flux calibration in a single band, we can exclude some of the flux standards from the analysis and use the excluded stars to see how well we recover their colors.

10. Software Implementation

TODO - new section on software implementation

Include : how do we calculate and apply color-correction terms, how do we use flat fields and illumination corrections, how/when do we run self-calibration and atmosphere fitting, and what do we report in DM (how do we store phi?)

10.1. Level 2 Data Products

11. Risks and Mitigations

The calibration process that we have designed is very similar to those of PS-1 and DES, as previously mentioned. It is therefore cause for some concern that the PS-1 results reported in (Tonry et al. 2012) are significantly poorer than we expect from our error analysis in Section 8. The need for the "tweak factor", and the lack of an explanation of its source, is of particular concern.

- Systematics error floor for photometry is higher than expected
- Forward models for illumination correction are less accurate than expected
- Stability of S_b^{sys} is less than expected

REFERENCES

Bergeron, P. 1992, JRASC, 86, 309

Bohlin, R. C., & Gilliland, R. L. 2004, AJ, 128, 3053

- Burke, D. L., et al. 2010, ApJ, 720, 811
- Eppeldauer, G. P., Yoon, H. W., Zong, Y., Larason, T. C., Smith, A., & Racz, M. 2009, Metrologia, 46, 139
- Frieman, J. A., et al. 2008, AJ, 135, 338
- Hansen, O. L., & Caimanque, L. 1975, PASP, 87, 935
- High, F. W., Stubbs, C. W., Rest, A., Stalder, B., & Challis, P. 2009, AJ, 138, 110
- Holberg, J. B., & Bergeron, P. 2006, AJ, 132, 1221
- Ivezić, Ž., et al. 2004, Astronomische Nachrichten, 325, 583
- . 2007, AJ, 134, 973
- Kurucz, R. L. 1993, VizieR Online Data Catalog, 6039, 0
- MacDonald, E. C., et al. 2004, MNRAS, 352, 1255
- Marshall, J. L., et al. 2013, ArXiv e-prints
- Nugent, P., Kim, A., & Perlmutter, S. 2002, PASP, 114, 803
- Padmanabhan, N., et al. 2008, ApJ, 674, 1217
- Radomski, J., Trancho, G., Fuhrman, L., Falvey, M., Gigoux, P., Montes, V., Daruich, F., & Lazo, M. 2010, in Society of Photo-Optical Instrumentation Engineers (SPIE) Conference Series, Vol. 7737, Society of Photo-Optical Instrumentation Engineers (SPIE) Conference Series
- Regnault, N., et al. 2009, A&A, 506, 999
- Schlafly, E. F., Finkbeiner, D. P., Schlegel, D. J., Jurić, M., Ivezić, Ž., Gibson, R. R., Knapp, G. R., & Weaver, B. A. 2010, ApJ, 725, 1175
- Schlafly, E. F., et al. 2012, ApJ, 756, 158
- Stubbs, C. W., Doherty, P., Cramer, C., Narayan, G., Brown, Y. J., Lykke, K. R., Woodward, J. T., & Tonry, J. L. 2010, ApJS, 191, 376
- Stubbs, C. W., & Tonry, J. L. 2012, ArXiv e-prints
- Stubbs, C. W., et al. 2007, PASP, 119, 1163

Tonry, J. L., et al. 2012, ApJ, 750, 99

Vanden Berk, D. E., et al. 2001, AJ, 122, 549

Veselovskii, I., Whiteman, D. N., Korenskiy, M., Kolgotin, A., Dubovik, O., & Perez-Ramirez, D. 2013, Atmospheric Measurement Techniques Discussions, 6, 3059

Wittman, D., Ryan, R., & Thorman, P. 2012, MNRAS, 421, 2251

A. Filter Set

Figure 38 illustrates the baseline LSST filter bandpasses, including a ‘standard’ atmosphere, and baseline estimates for the mirrors, lenses, filter and detector transmission and sensitivity functions.

B. Photometric measurements for non-main sequence stars

LSST will record a series of m_b^{nat} measurements for each astronomical object in each visit. These m_b^{nat} measurements are generated directly from the counts recorded in each image, corrected with the photometrically uniform, broad-band flat field and for gray (cloud) atmospheric extinction effects. However, these m_b^{nat} measurements will vary as the shape of the bandpass changes, whether as a function of position in the focal plane or as a function of changes in atmospheric absorption components. Correcting for these effects requires assuming a particular SED for each source, and produces m_b^{std} values after applying Δm_b^{meas} offsets (see the overview of calibration in section 5 for a review).

For most objects, LSST will simply assume the source has a flat SED, which means that m_b^{std} is exactly equal to m_b^{nat} , as by definition then Δm_b^{meas} is zero. To permit scientists to generate higher precision photometry for objects using arbitrary SEDs, LSST must provide a record of $\phi_b^{meas}(\lambda, alt, az, x, y, t)$ as well as the normalization zeropoint offsets for each observation. With these additional pieces of information, scientists can generate more appropriate Δm_b^{meas} corrections, using their own chosen object SED to generate m_b^{std} . Sections ?? and ?? outline the typical magnitudes of these corrections for main sequence stars; Δm_b^{meas} can easily be on the order of 20 mmag for *gri*, or even 100 mmag in *u* band. For more extreme SEDs, these corrections may be even larger.

Figure 40 illustrates the likely magnitude of these Δm_b^{meas} corrections for a wide variety of SEDs. In each plot, the main sequence stars are shown as in the figures in the main paper (small dots, color-coded by metallicity), although given the increased scale here they only appear as a purple series of circles. M dwarfs are now included, generally mimicking the behavior of the main sequence stars but extending further into the red. More unusual SEDs are also included; a quasar SED, based on a composite of many empirical quasars from SDSS from Vanden Berk et al. (2001) that has been extended to the full LSST wavelength range through the addition of power law flux above and below the original range ($f_\nu \propto 1/\lambda^{0.5}$ for $\lambda < 89\text{nm}$ & $f_\nu \propto 1/\lambda^{1.5}$ for $\lambda > 800\text{nm}$), and redshifted from $z = 0$ to $z = 3$; also a sample of SN Ia from templates generated by Peter Nugent (Nugent et al. 2002), redshifted from $z = 0$ to $z = 1$.

The figure shows the Δm_b^{meas} values that would be expected under a maximum change of atmospheric parameters and under a likely bandpass shift. This demonstrates how much the reported m_b^{nat} values could vary for each object. If LSST was to just calculate an offset between m_b^{nat} and m_b^{std} based on an object’s color (and assuming that the object had an SED similar to a main sequence star), the resulting m_b^{std} values would be incorrect by the value of the offset between the true Δm_b^{meas} for the SED and the main sequence Δm_b^{meas} values at each color; this could easily be more than 20mmag.

With the wide variety of objects and SEDs that will be possible in the LSST data set, it is crucial to provide the information and tools so that scientists may calculate highly precise m_b^{std} magnitudes for their objects of interest. This means recording or providing the means to recalculate $\phi_b^{sys+atm}(\lambda, t)$ for every object detected with LSST.

C. Glossary

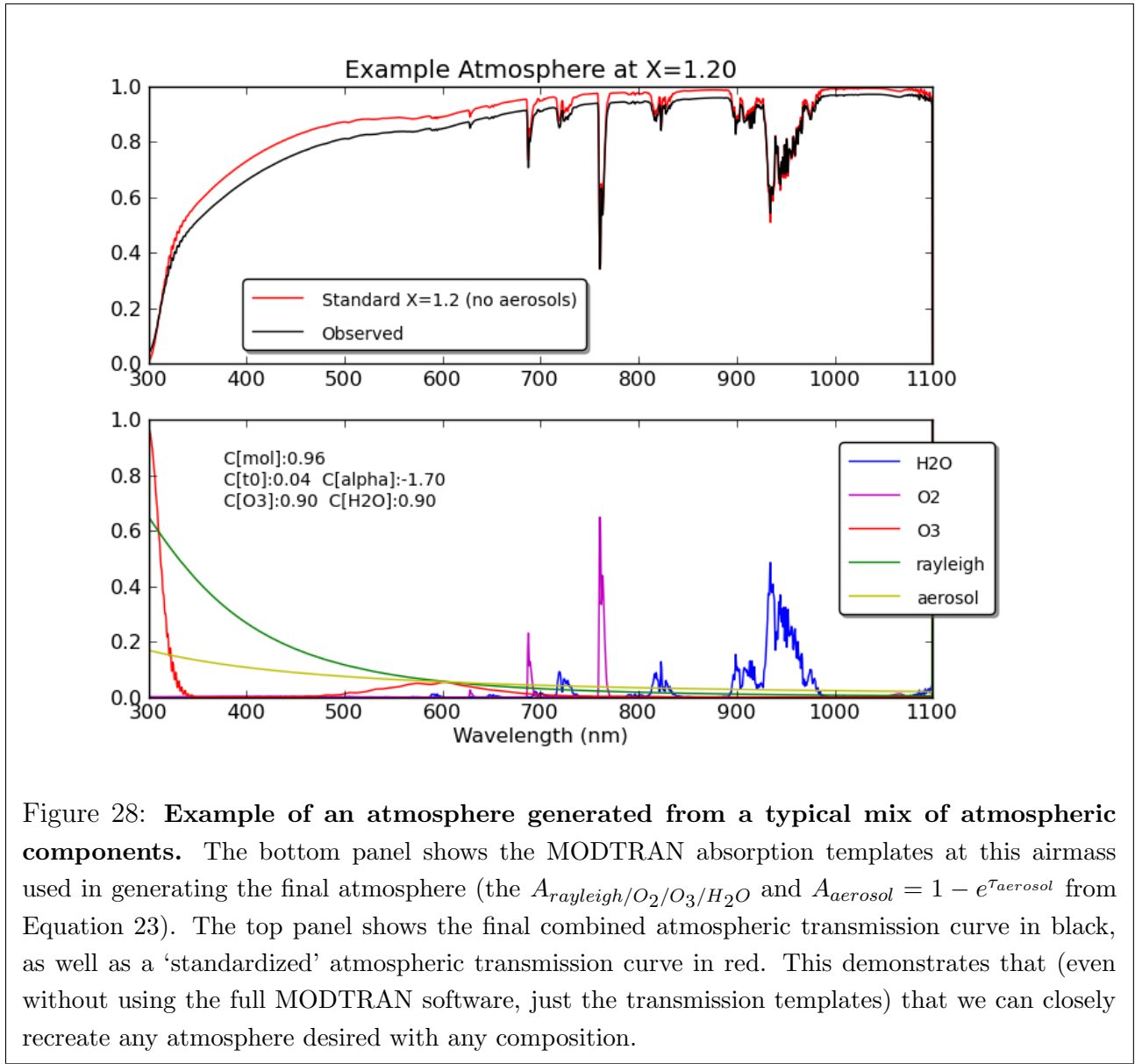
- **Level 1 Data Product.** A data product, such as a measurement of an astronomical object’s position or flux in a single image, that is computed on a nightly basis. Level 1 data products primarily consist of alerts on transient, variable and moving objects. The photometric calibration process outlined in this paper does not apply to Level 1 data products. Level 1 data products will be calibrated using all applicable prior knowledge (including secondary standard catalogs generated from previous Data Release calibration of all LSST-observed stars in the field).
- **Level 2 Data Product.** A data product, such a measurement of an astronomical object’s position or flux in either a single image or a series of images, that is computed on the Data Release schedule, on a six-month or yearly schedule. Level 2 data products leverage all previous observations of the same object, as well as all knowledge of the LSST system accumulated to that point. The photometric calibration process outlined in this paper is used to generate Level 2 data products.
- **Normalized system response, $\phi_b(\lambda)$.** The normalized system response describes the shape of the bandpass transmission curve, separating this from the normalization of the throughput curve which can be determined separately. $\phi_b(\lambda)$ is described by Equation 5. The integral of $\phi_b(\lambda)$ is always 1.
- **Camera Calibration Optical Bench (CCOB).** The CCOB is an apparatus to calibrate the spatial and wavelength-dependent response of the focal plane (detector + camera). The CCOB uses a well controlled, wavelength-variable, light source (such as a tuneable laser) calibrated using a NIST photodiode to illuminate the focal plane

when the camera is unmounted from the telescope. This light source, which produces a spot in the focal plane approximately the size of or smaller than the PSF, will be scanned across the detector (x, y) at a variety of beam incident angles, (θ, ϕ) and at a variety of wavelengths (λ). This allows the response of the detector to be measured in the presence of a well-understood light source. The response of the detector can be measured in two different configurations: one with only the detector and the dewar window - which doubles as lens 3 (L3) - and one with the detector, L3, L2, L1, a small test-section of filter and the camera shutter. The filter test section used is not the full LSST filter, and thus will not capture spatial non-uniformities in the filter bandpass. The CCOB provides test data about the camera assembly for camera acceptance and will help constrain the optical ZEMAX model, although without a full filter it cannot capture the full set of parameter required for the ZEMAX model. More details about the requirements and physical apparatus of the CCOB are available in LSST-10015 and LSST-8217.

- **Broadband flat field.** An image obtained by observing a light source which generates photons with a wide range of wavelengths (as opposed to a narrow-band flat), with relatively uniform illumination across the field of view. Night sky flats, twilight flats, and white-light or broadband dome screen flats would all generate broadband flat fields.
- **Narrow-band flat field.** An image obtained by observing a light source which generates photons with a very narrow range of wavelengths (hypothetically, even a single wavelength), with relatively uniform illumination across the field of view. A dome screen illuminated with a narrow-band laser light source will generate a narrow-band flat field.
- **‘Observed’ flat field.** A flat field, as obtained by observing the dome screen projectors. Generally would refer to a broadband flat field.
- **Photometric flat field.** A flat field which produces uniform photometric measurements across the field of view for a flat $F_\nu(\lambda)$ source. A photometric flat field must be based on a broadband flat.
- **Illumination Correction.** The ratio between the photometric flat field and the observed flat field.

$$\text{Flat}_{\text{photometric}} = \text{Flat}_{\text{observed}} * \text{IlluminationCorrection} \quad (\text{C1})$$

- **Natural magnitude.** A magnitude measurement which relates directly to the number of counts measurement in an image (after including a photometric flat field correction and a rough zeropoint for an entire image). The natural magnitude relate to an ADU count that does *not* account for the color or SED of the source being observed, thus does not include any wavelength-dependent corrections. For a non-variable source observed under variable atmospheric transmission conditions and/or at varying locations in the field of view, the natural magnitude reported will change due to changes in the bandpass shape. The natural magnitude is equivalent to an observed magnitude, after the appropriate zeropoints have been applied.
- **Standard magnitude.** A magnitude measurement which includes not only corrections for the photometric flat field and a rough zeropoint for the image, but also includes a correction for wavelength-dependent effects. This means the Δm_b^{meas} appropriate to correct the natural magnitude of the object from the observed bandpass shape, $\phi_b^{meas}(\lambda, t)$, to the standard bandpass shape, $\phi_b^{std}(\lambda)$, has been calculated for the SED of the object and applied. For a non-variable source, m_b^{std} will be constant over time even if the atmospheric absorption curve or the location in the field of view changes.
- **Operations Simulation.** The Operations Simulation is a simulated pointing history of LSST, covering the sky in the same manner as the telescope could, in practice. It uses weather conditions based on historical records from Cerro Tololo, including appropriate seeing and sky brightness variations. The motion of the telescope is simulated in high fidelity, including acceleration from field to field and cable wrap. A variety of proposals are used to determine which fields to observe at each time; these proposal include the ‘universal cadence’ (satisfying most of LSST’s science requirements) and ‘deep drilling’ (a limited set of fields, observed frequently and deeply over the lifetime of the survey).
- **PWV.** Precipitable Water Vapor. The total column depth of water vapor in the atmosphere, measured at zenith. The units are mm of liquid water equivalent.



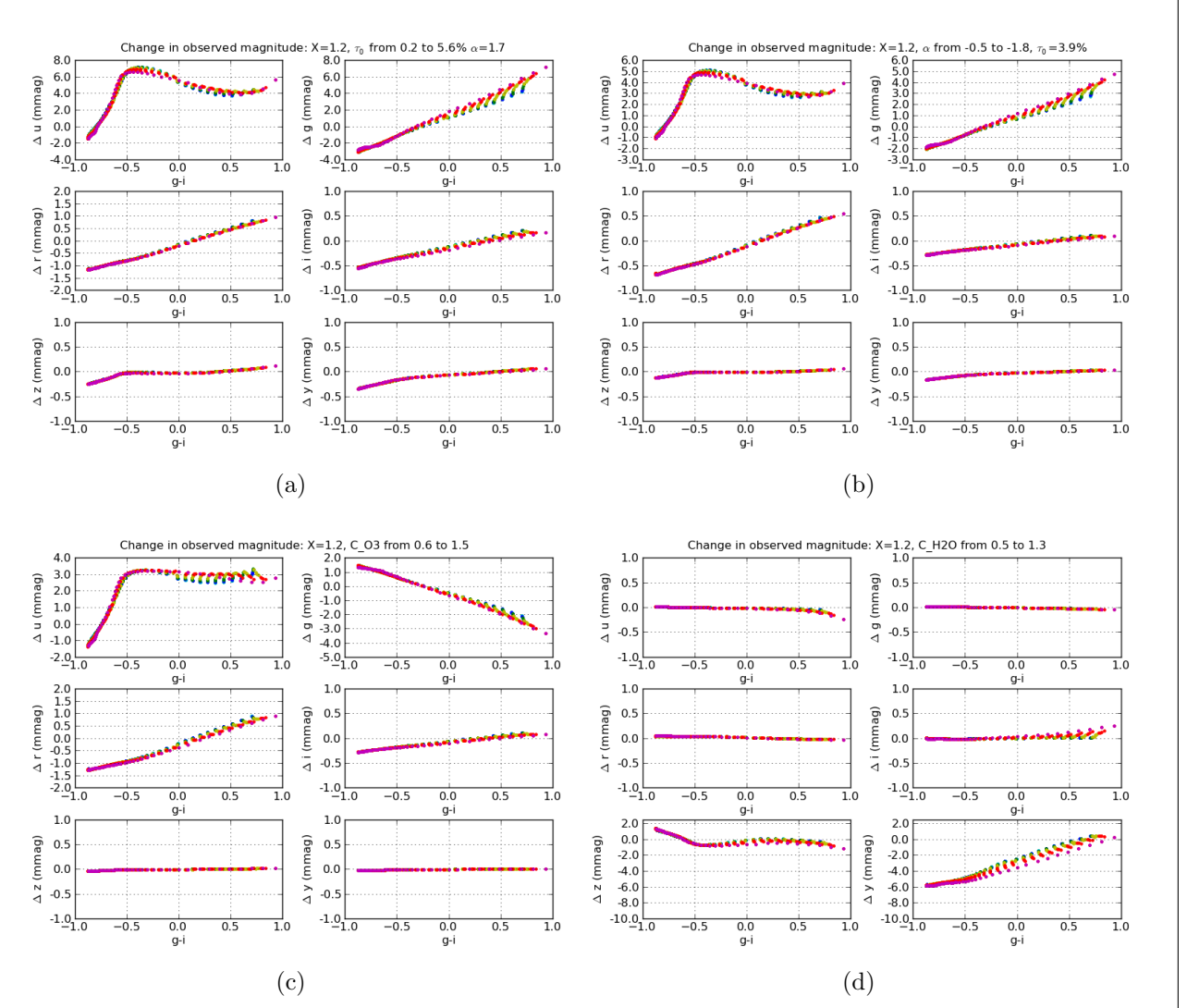
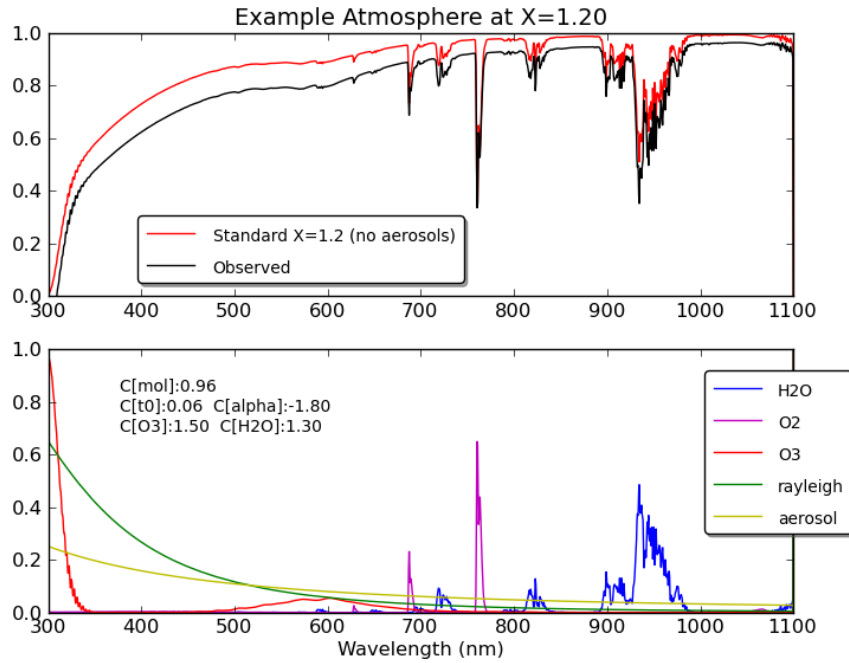
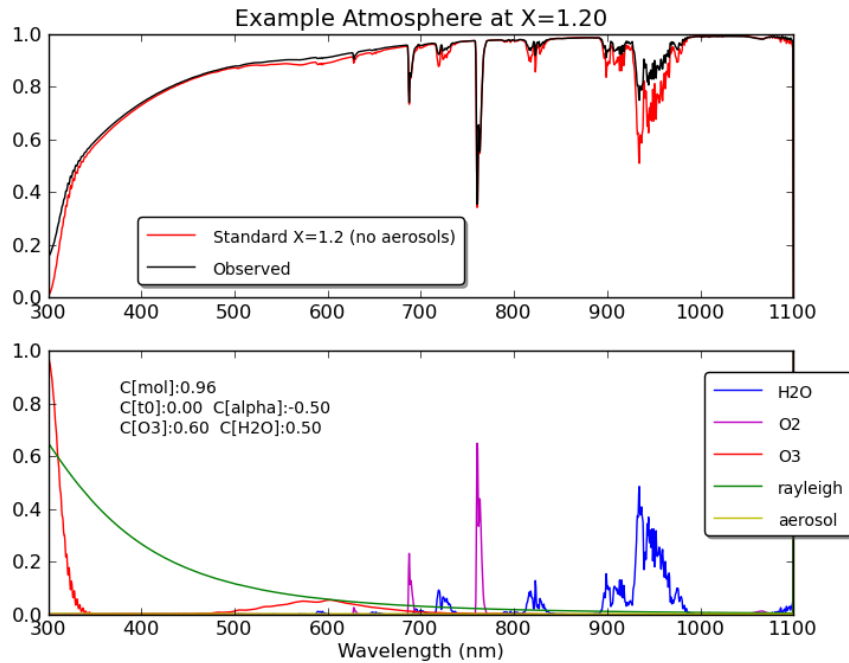


Figure 29: Δm_b^{obs} due to variations of each individual absorption component. Each atmospheric transmission curve (at $X=1.2$) was combined with the set of main sequence Kurucz curves to determine the resulting changes in observed magnitudes, as in Figure 25. Panels 36a and 36b show the effects of varying aerosol absorption in τ_0 and α respectively, Panel 29c shows the effect of varying O_3 absorption. These effects are concentrated in u and g bands, with a negligible effect in izy . Panel 29d shows the effect of varying the H_2O absorption, which is strongest in y , with some effect in z and no effect in $ugri$.



(a)



(b)

Figure 30: ‘Extreme’ atmospheres generated from MODTRAN profiles and extremes of atmospheric coefficients. Using the extremes of C_{H_2O} , C_{O_3} , and τ_0 and α from Burke et al. (2010), two test atmospheres with $X = 1.2$ were created using Equation 23.

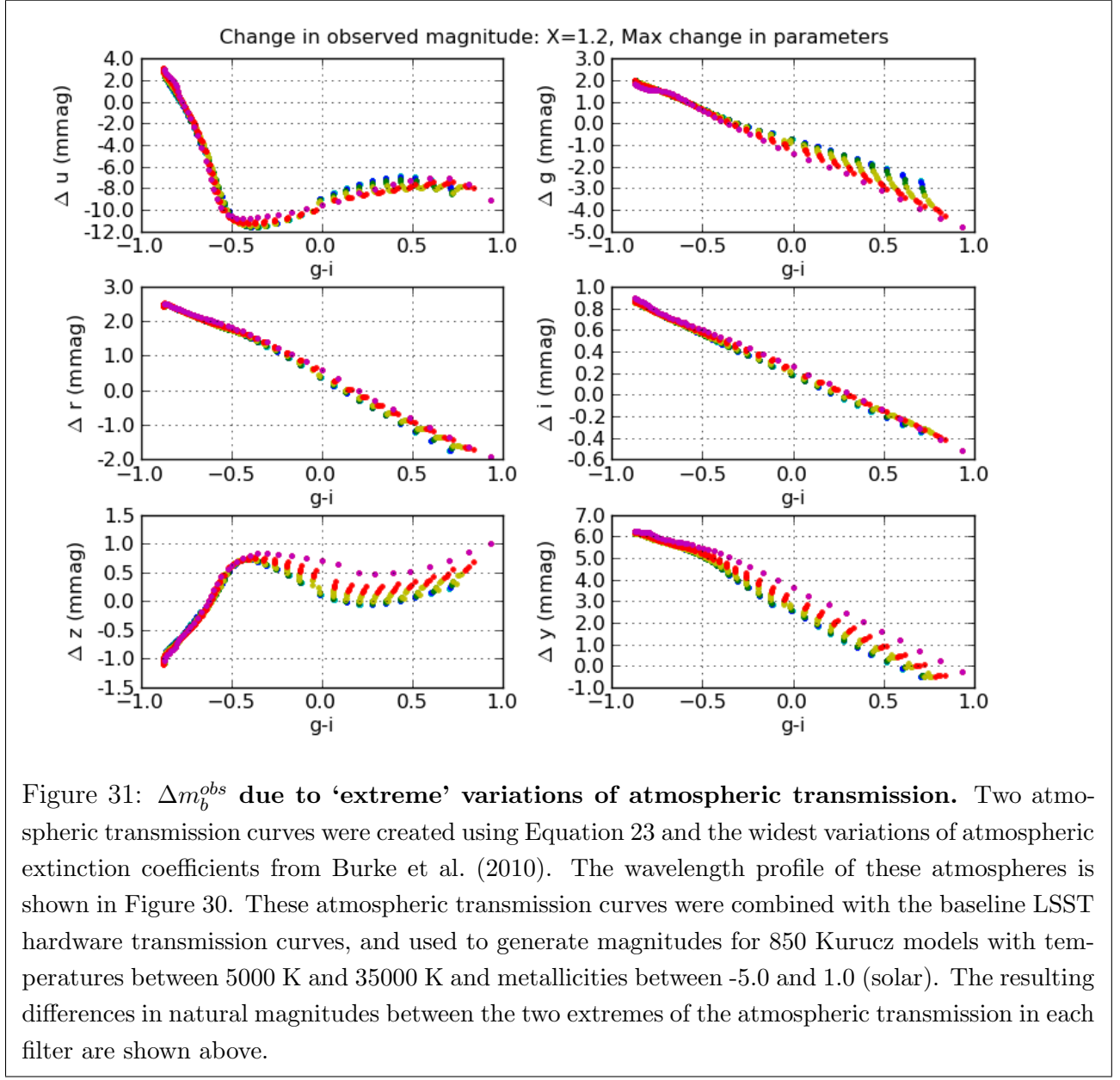
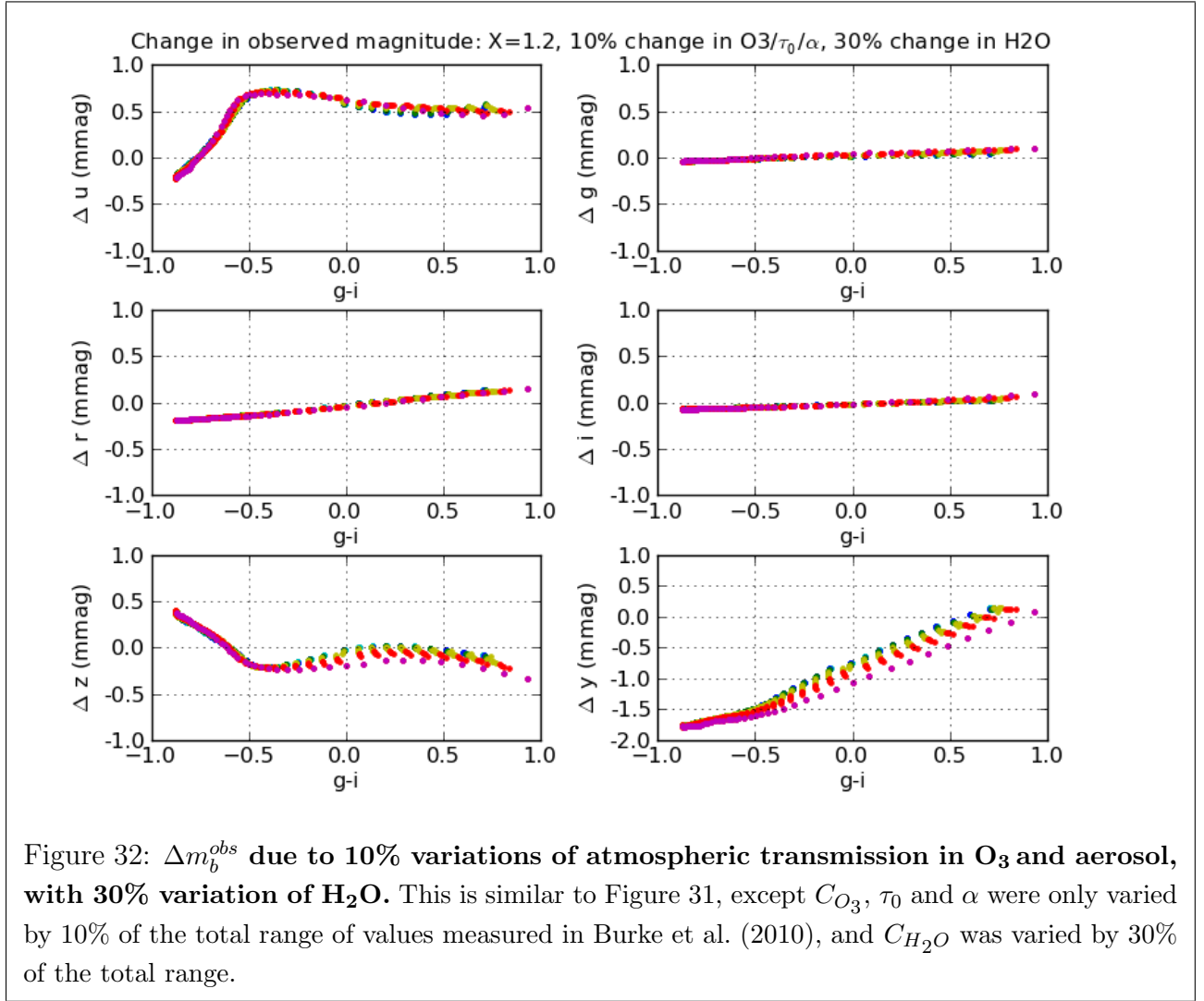
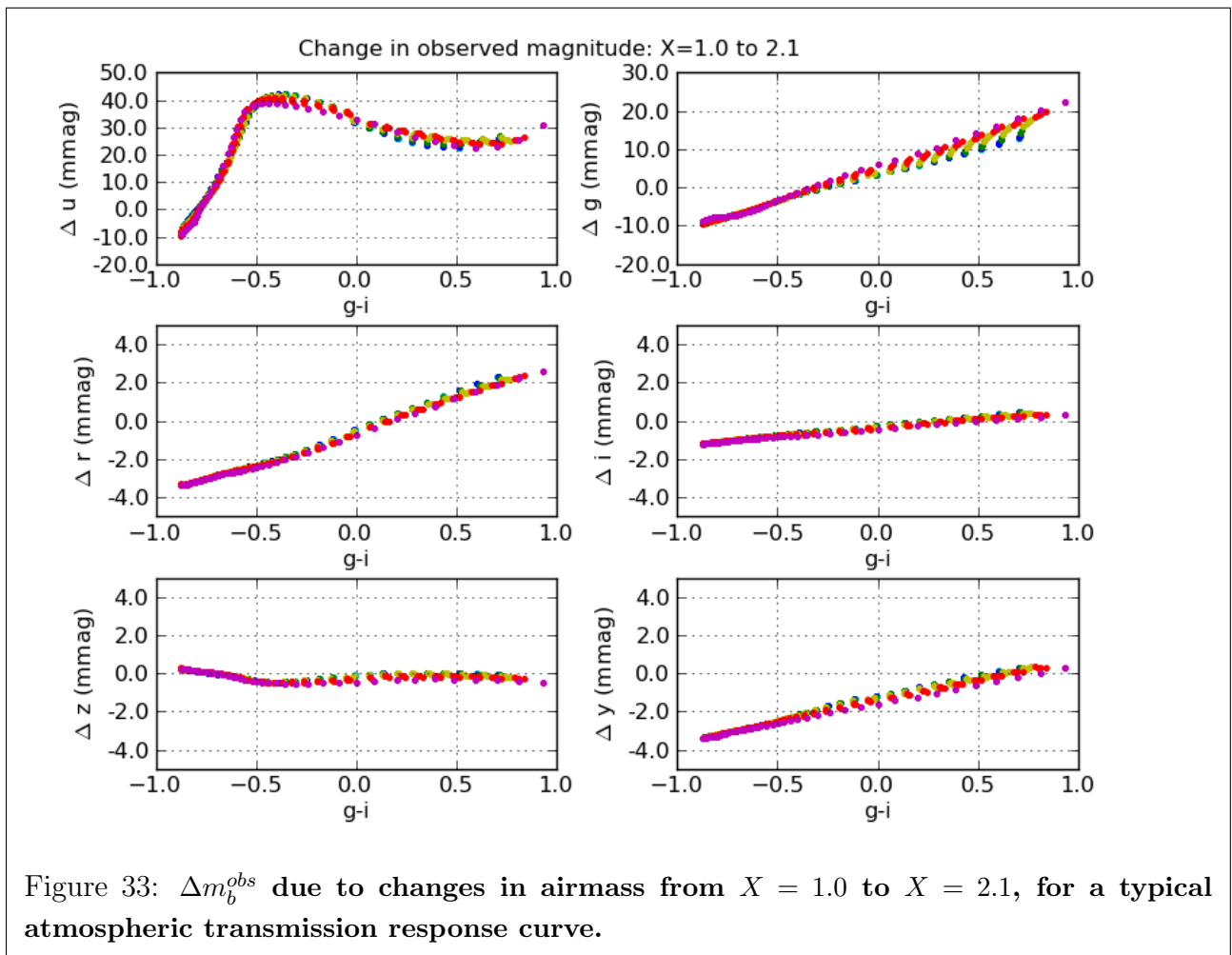
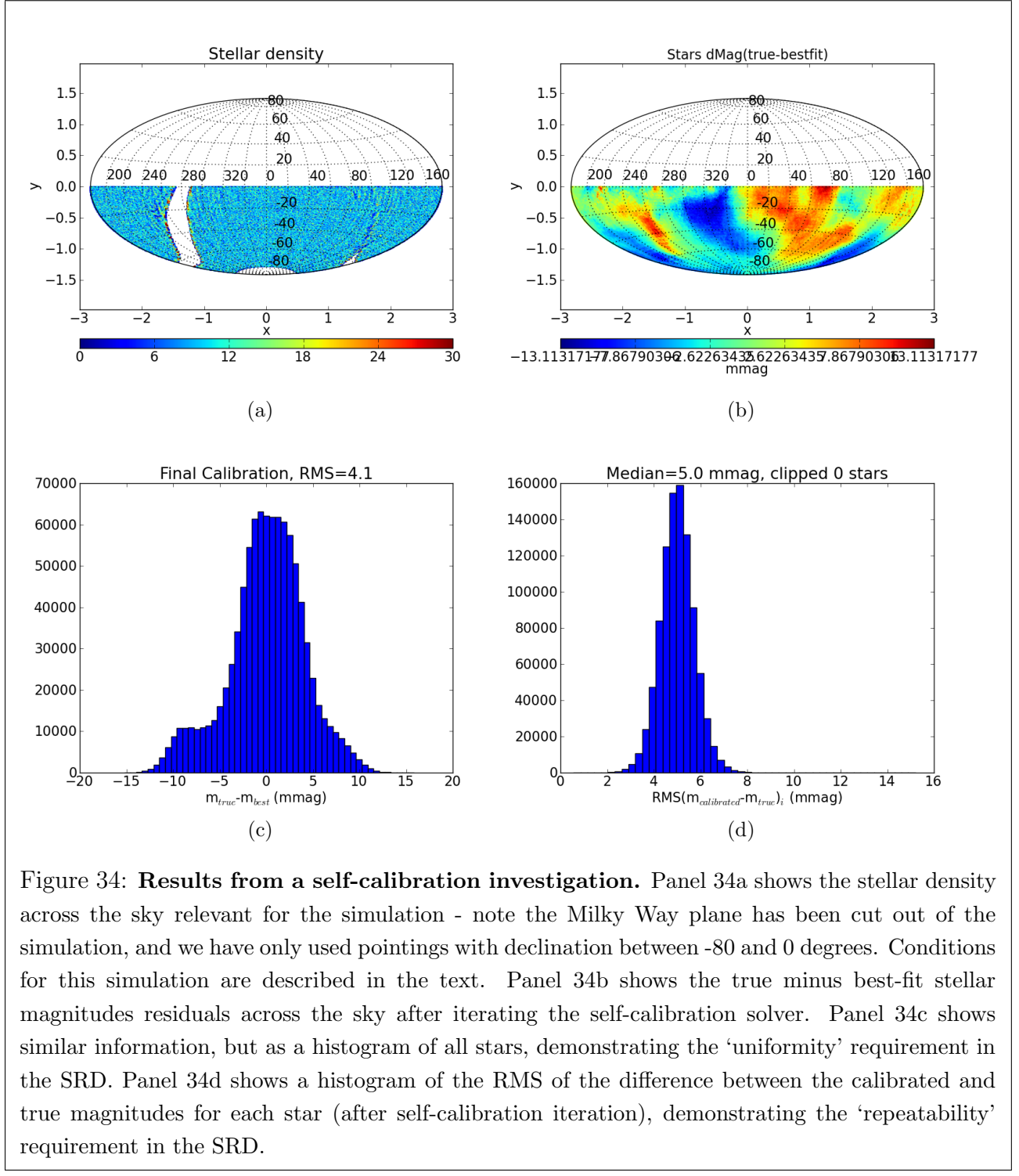


Figure 31: Δm_b^{obs} due to ‘extreme’ variations of atmospheric transmission. Two atmospheric transmission curves were created using Equation 23 and the widest variations of atmospheric extinction coefficients from Burke et al. (2010). The wavelength profile of these atmospheres is shown in Figure 30. These atmospheric transmission curves were combined with the baseline LSST hardware transmission curves, and used to generate magnitudes for 850 Kurucz models with temperatures between 5000 K and 35000 K and metallicities between -5.0 and 1.0 (solar). The resulting differences in natural magnitudes between the two extremes of the atmospheric transmission in each filter are shown above.







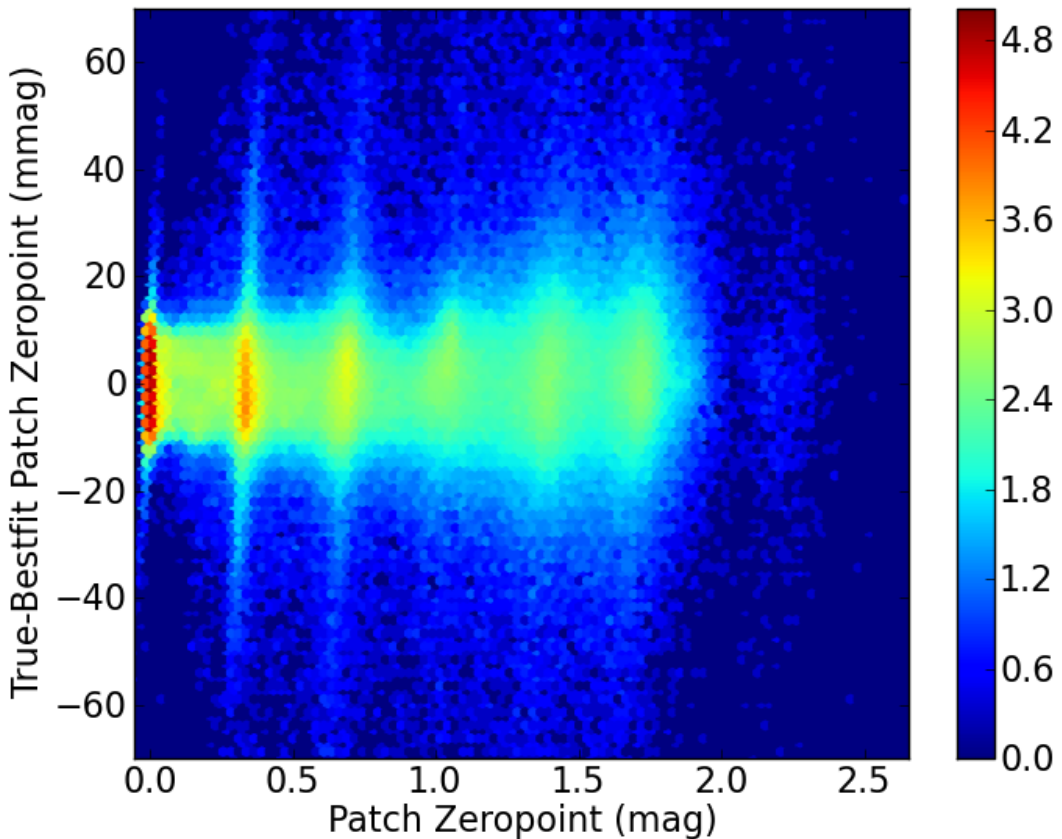


Figure 35: Zeropoint errors vs zeropoint, from a self calibration simulation. The color scale shows the \log_{10} of the number of samples at that point. The periodic behavior of the zeropoint density is an artifact of OpSim’s treatment of cloud cover.

